

# Structures, Interconversions, and Spectroscopy of Iron Carbonyl Clusters with an Interstitial Carbide: Localized Metal Center Reduction by Overall Cluster Oxidation

Subramaniam Kuppaswamy,<sup>†</sup> Joshua D. Wofford,<sup>‡</sup> Chris Joseph,<sup>†</sup> Zhu-Lin Xie,<sup>†</sup> Azim K. Ali,<sup>†</sup> Vincent M. Lynch,<sup>†</sup> Paul A. Lindahl,<sup>‡</sup> and Michael J. Rose<sup>\*,†</sup>

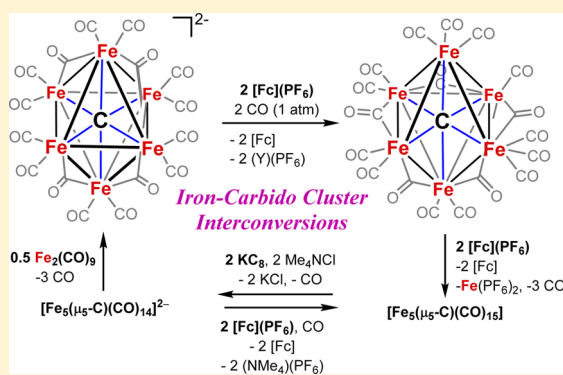
<sup>†</sup>Department of Chemistry, The University of Texas at Austin, Austin, Texas 78712, United States

<sup>‡</sup>Department of Chemistry, Texas A&M University, College Station, Texas 77840, United States

## S Supporting Information

**ABSTRACT:** The syntheses, interconversions, and spectroscopic properties of a set of iron carbonyl clusters containing an interstitial carbide are reported. This includes the low temperature X-ray structures of the six-iron clusters  $(Y)_2[Fe_6(\mu_6-C)(\mu_2-CO)_4(CO)_{12}]$  (1a–c; where Y = NMe<sub>4</sub>, NEt<sub>4</sub>, PPh<sub>4</sub>); the five-iron cluster  $[Fe_5(\mu_5-C)(CO)_{15}]$  (3); and the novel formulation of the five-iron cluster  $(NMe_4)_2[Fe_5(\mu_5-C)(\mu_2-CO)(CO)_{13}]$  (4). Also included in this set is the novel charge-neutral cluster,  $[Fe_6(\mu_6-C)(CO)_{18}]$  (2), for which we were unable to obtain a crystallographic structure. As synthetic proof for the identity of 2, we performed a closed loop of interconversions within a family of crystallographically defined species (1, 3, and 4):  $[Fe_6]^{2-} \rightarrow [Fe_6]^0 \rightarrow [Fe_5]^0 \rightarrow [Fe_5]^{2-} \rightarrow [Fe_6]^{2-}$ . The structural, spectroscopic, and electronic properties of this “missing link” cluster 2 were investigated by IR, Raman, XPS, and Mössbauer spectroscopies—

as well as by DFT calculations. A single  $\nu_{CO}$  feature ( $1965\text{ cm}^{-1}$ ) in the IR spectrum of 2, as well as a prominent Raman feature ( $\nu_{\text{symm}} = 1550\text{ cm}^{-1}$ ), are consistent with the presence of terminal carbonyls and a  $\{(\mu_6-C)Fe_6\}$  arrangement of iron centers around the central carbide. The XPS of 2 exhibits a higher energy Fe 2p<sub>3/2</sub> feature (707.4 eV) as compared to that of 1 (705.5 eV), consistent with the two-electron oxidation induced by treatment of 1 with two equivalents of  $[Fc](PF_6)$  under CO atmosphere (for the two added CO ligands). DFT calculations indicate two axial and four equatorial Fe sites in 1, all of which have the same or similar oxidation states, for example, two Fe(0) and four Fe(+0.5). These assignments are supported by Mössbauer spectra for 1, which exhibit two closely spaced quadrupole doublets with  $\delta = 0.076$  and  $0.064\text{ mm s}^{-1}$ . The high-field Mössbauer spectrum of 2 (4.2 K) exhibits three prominent quadrupole doublets with  $\delta = -0.18$ ,  $-0.11$ , and  $+0.41\text{ mm s}^{-1}$ . This indicates three pairs of chemically equivalent Fe sites. The first two pairs arise from irons of a similar oxidation state, while the last pair arises from irons in a different oxidation state, indicating a mixed-valent cluster. Variable field Mössbauer spectra for 2 were simulated assuming these two groups and a diamagnetic ground state. Taken together, the Mössbauer results and DFT calculations for 2 indicate two axial Fe(II) sites and four equatorial sites of lower valence, probably Fe(0). In the DFT optimized pentagonal bipyramidal structure for 2, the Fe(II)–C<sub>carbide</sub> distances are compressed ( $\sim 1.84\text{ \AA}$ ), while the Fe(0)–C<sub>carbide</sub> distances are elongated ( $\sim 2.05\text{ \AA}$ ). Analysis of the formulations for 1 (closo-square bipyramid) and 2 (nido-pentagonal bipyramid) is considered in the context of the textbook electron-counting rules of  $14n+2$  and  $14n+4$  for closo and nido clusters, respectively. This redox-dependent intracuster disproportionation of Fe oxidation states is concluded to arise from changes in bonding to the central carbide. A similar phenomenon may be promoted by the central carbide of the FeMoco cluster of nitrogenase, which may in turn stimulate N<sub>2</sub> reduction.



## INTRODUCTION

Polymetallic clusters of the 4d and 5d metals rarely present an opportunity to study paramagnetic species, especially even-electron systems, due to the high energetic penalty for spin unpairing in the greater ligand field of heavy metals. For example, the closest ruthenium congener of the neutral iron-carbido cluster described in this work,  $[Ru_6(\mu_6-C)(CO)_{17}]$ , is diamagnetic.<sup>1</sup> Such metal-carbide clusters have been utilized as catalysts for chemical transformations such as alkene isomer-

ization, alkene hydrogenation, Fischer–Tropsch synthesis, and the hydrogenation of amides. Such clusters have also been investigated as low-temperature catalysts for the water–gas-shift reaction.<sup>2–7</sup> Nitrogenase, the enzyme that catalyzes the six-electron reduction of dinitrogen (N<sub>2</sub>) to ammonia (NH<sub>3</sub>),<sup>8–11</sup> contains a carbide in the center of the active site FeMoco

Received: March 29, 2017

cluster.<sup>10,11</sup> Indeed, a recent review by Holland has delineated a number of recent attempts at synthetically modeling this complex bioinorganic target.<sup>12</sup>

In the cases of iron carbonyl clusters and iron-carbido carbonyl clusters, the ground states of nearly all isolated clusters are diamagnetic due to the strong antiferromagnetic coupling between equivalent Fe centers, as well as the low-spin configurations enforced by carbonyl (CO) ligands. There have been limited reports of iron-carbido carbonyl clusters since the 1960s, all of which have focused on the isolation and characterization of multi-Fe clusters. Indeed, the nucleophilic carbide ( $C^{4-}$ ) is a potential building unit to assemble polymetallic clusters via covalent bonds between a central carbide and metal atoms, thus enforcing strong metal–metal bonds within the cluster.<sup>13–16</sup> Both of the electrons stored in the chemical bonds between (or among) metal ions and open coordination sites have been employed to achieve chemical transformations such as proton reduction<sup>17</sup> or reactions related to Fischer–Tropsch chemistry.<sup>18</sup>

In recent years, iron-mediated catalytic reactions have received much attention as promising alternatives for noble metal catalysts.<sup>5–7</sup> In the nitrogenase cofactor, the central carbide ligand that holds multiple iron atoms in a discrete cluster may serve to improve multielectron redox processes with minimal structural changes. Moreover, an interstitial carbide atom encapsulated within a multimetallic cluster can provide stability to the cluster core to prevent fragmentation or large structural changes during catalytic turnover.

In 1962, Braye and co-workers first characterized an interstitial carbide atom encapsulated in a discrete five-iron carbonyl cluster.<sup>19</sup> A decade later, Churchill and co-workers reported the corresponding dianionic six-iron cluster of formula  $[Fe_6(\mu_6-C)(\mu_2-CO)_4(CO)_{12}]^{2-}$  (**1** in this report) via degradation of the heterometallic anion  $[MnFe_2(CO)_{12}]^-$ . At that time, the room-temperature low-resolution X-ray structure of **1** did not satisfactorily describe the connectivity or bond metrics of the bridging carbonyls.<sup>20,21</sup> Interestingly, the  $[Fe_6]^{2-}$  cluster has since been utilized as an inorganic synthon to prepare the corresponding lower nuclearity cluster complexes, in which the central carbide remains bound to the remaining metal ions.<sup>22,23</sup> Lower nuclearity clusters (five- and four-iron clusters) have since been investigated to explore the “open-face”  $Fe_n-C$  bonding motif as analogues of heterogeneous catalytic systems. Remarkably, the carbide encapsulation stabilizes  $[Fe_6]^{2-}$  core under either an electrophilic substitution with  $[Au(PPh_3)]^+$  or ligand replacement with nitrous oxide and sulfur dioxide, respectively.<sup>24–26</sup> However, chemical oxidation of  $[Fe_6]^{2-}$  with halide-containing oxidants and/or acidic workup yielded lower nuclearity clusters via the oxidative elimination of  $\{Fe(CO)_m(X)_n\}$  units.<sup>22</sup> It is likely that the increase of oxidation state coupled to the presence of halides (and in the absence of chelating ligands) decreases the metal–metal bond strength, thus leading to degradation of the six-iron cluster. However, there are few reports regarding the “pure” redox activity of  $[Fe_6]^{2-}$  clusters, although Berben and co-workers have recently investigated both proton reduction and  $CO_2$  electrocatalysis of nitride-based iron carbonyl clusters.<sup>27,28</sup> Herein, we utilize a known series of five- and six-iron clusters to prepare and study the “missing link” cluster in this series, the six-iron neutral cluster  $[Fe_6(\mu_6-C)(CO)_{18}]$  (**2**).

To further utilize and characterize the six-iron core for multielectron redox reactions, we have initiated a research program to address the multielectron redox transformations of

first-row transition metal clusters. In this Article, we report a convenient synthetic route for hexa-iron cluster anions with varying cations ( $NMe_4$ ,  $NEt_4$ , and  $PPh_4$ ). These clusters provide more precise data sets of X-ray structure determinations with respect to the nature and number of the bridging carbonyls. In addition, controlled oxidation of  $[Fe_6]^{2-}$  with an outer-sphere redox reagent provides the first access to the oxidized  $[Fe_6]^0$  cluster (**2**). Spectroscopic characterization of **2** and its interconversions among  $[Fe_6]^{2-}$ ,  $[Fe_5]^0$ , and  $[Fe_5]^{2-}$  confirm its identity.

## EXPERIMENTAL SECTION

**Reagents and Procedures.** All manipulations were performed under an inert atmosphere using Schlenk line or glovebox techniques. HPLC grade solvents were purchased from EMD, Fisher, Macron, or J.T. Baker, and dried through an alumina column system (Pure Process Technology). Deuterated solvents ( $d^6$ -benzene,  $d^8$ -THF) were purchased from Cambridge Isotopes or Acros Organics and used as received. Diglyme,  $NEt_4Cl \cdot H_2O$ ,  $[Fe(CO)_5]$ ,  $FeCl_3 \cdot 6H_2O$ , ferrocenium hexafluorophosphate, iodine,  $NMe_4Cl$ , naphthalene, and  $PPh_4Cl$  were used as received. The iron synthons  $Na_2[Fe(CO)_4]$  and solutions of  $Na_2[Fe_6(\mu_6-C)(CO)_{16}]$  were prepared according to modified literature reports.<sup>22,29</sup>

Caution: Iron carbonyls are extremely toxic, and disodium tetracarbonylferrate is pyrophoric. These materials should be handled carefully in a drybox or well-ventilated fume hood under inert atmosphere.

**Optimized Preparation of  $[Na_2Fe(CO)_4]$ .** A solution of naphthalene (9.5 g, 74 mmol) in THF (100 mL) was chilled at  $-78^\circ C$ , and sodium pieces (1.7 g, 79 mmol) were slowly added. The resulting mixture was gradually warmed to room temperature and stirred for 2 h to ensure complete in situ formation of the green sodium naphthalenide. The reaction mixture was again chilled to ice-cold temperature, and to this neat  $[Fe(CO)_5]$  (5.0 mL, 37 mmol) was added dropwise over a period of 5–10 min. The reaction mixture was stirred at room temperature for 2 h, and the solution turned red-brown. All volatiles were removed in vacuo, and the crude residue was redissolved in THF; subsequent dilution of the mixture with cold pentane precipitated the analytically pure product. The reddish brown precipitate of disodium ferrate was isolated by filtration and dried under vacuum for 30 min. The product was stored at  $-20^\circ C$  under argon atmosphere until use. Yield: 7.5 g (95%). IR (solid state):  $1762\text{ cm}^{-1}$ .

**$(NMe_4)_2[Fe_6(\mu_6-C)(\mu_2-CO)_4(CO)_{12}]$  (**1a**).**<sup>22</sup> A neat aliquot of  $[Fe(CO)_5]$  (5.0 mL, 37 mmol) was added dropwise to a solution of  $[Na_2Fe(CO)_4]$  (1.56 g, 7.32 mmol) in diglyme (25 mL) under  $N_2$  atmosphere at room temperature over a period of 5 min. The resulting mixture was refluxed at  $160^\circ C$  for 6 h, resulting in a violet solution with concomitant elimination of CO gas. The mixture was then gradually cooled to room temperature and subsequently washed with hexanes ( $3 \times 30\text{ mL}$ ) to remove any organic-soluble impurities, to obtain the dark violet residue of disodium salt of  $Na_2[Fe_6(\mu_6-C)(CO)_{16}]$ . This material was then extracted with degassed water (400 mL); to this was added a solution of  $NMe_4Cl$  (1.77 g, 16.1 mmol) in degassed water (50 mL) dropwise at room temperature over a period of 2 h. During this process, microcrystalline **1a** was precipitated, and the resulting mixture was stirred at room temperature for 12 h. The purple materials of **1a** were filtered out via a medium-pore-size PYREX glass frit over a thick pad of Celite. The crude material was washed with  $Et_2O$  and then extracted into THF (100 mL). Removal of solvent in vacuo afforded a violet crystalline material of **1a**. Yield: 3.8 g (51%). X-ray quality crystals of **1a** were grown by vapor diffusion of pentane into a THF solution of **1a** at  $-20^\circ C$ .  $^1H$  NMR (400 MHz,  $d^8$ -THF, ppm) (Figure S1):  $\delta$  3.21 ( $CH_3$ , bs).  $^{13}C\{^1H\}$  NMR (100.5 MHz,  $d^8$ -THF, ppm) (Figure S2):  $\delta$  484.7 ( $\mu_6-C$ ), 229.2 (CO), 56.0 ( $CH_3$ ). UV/vis in nm ( $\epsilon = L\text{ mol}^{-1}\text{ cm}^{-1}$ ) (Figure S3): 520 (3920). IR (solid state) (Figure S4): 1910, 1730  $\text{cm}^{-1}$ . Anal. Calcd for  $C_{29}H_{32}N_2O_{17}Fe_6$ : C, 34.29; H, 3.18; N, 2.76. Found: C, 33.93; H, 3.18; N, 2.87.

( $\text{NEt}_4$ )<sub>2</sub>[ $\text{Fe}_6(\mu_6\text{-C})(\mu_2\text{-CO})_4(\text{CO})_{12}$ ] (**1b**). The same procedure as for **1a** was followed, except that  $\text{NEt}_4\text{Cl}\cdot\text{H}_2\text{O}$  (2.96 g, 16.1 mmol) was substituted for  $\text{NMe}_4\text{Cl}$ . Yield: 44% (3.6 g). X-ray quality single crystals of **1b** were grown by vapor diffusion of pentane into a THF solution of **1b** at  $-20^\circ\text{C}$ .  $^1\text{H}$  NMR (400 MHz,  $d^8$ -THF, ppm) (Figure S5):  $\delta$  3.32 ( $\text{CH}_2$ , 2H, bs), 1.33 ( $\text{CH}_3$ , 3H, bs).  $^{13}\text{C}\{^1\text{H}\}$  NMR (100.5 MHz,  $d^8$ -THF, ppm) (Figure S6):  $\delta$  484.7 ( $\mu_6\text{-C}$ ), 229.2 (CO), 53.2 ( $\text{CH}_2$ ), 7.7 ( $\text{CH}_3$ ). UV/vis in nm ( $\epsilon = \text{L mol}^{-1} \text{cm}^{-1}$ ) (Figure 7): 520 (3410). IR (solid state) (Figure 8): 1901, 1742  $\text{cm}^{-1}$ . Anal. Calcd for  $\text{C}_{37}\text{H}_{48}\text{N}_2\text{O}_{17}\text{Fe}_6$ : C, 39.40; H, 4.29; N, 2.48. Found: C, 39.96; H, 4.27; N, 2.54.

( $\text{PPh}_4$ )<sub>2</sub>[ $\text{Fe}_6(\mu_6\text{-C})(\mu_2\text{-CO})_4(\text{CO})_{12}$ ] (**1c**). The same procedure as for **1a** was followed, except that  $\text{PPh}_4\text{Cl}$  (2.2 g, 5.8 mmol) was substituted for  $\text{NMe}_4\text{Cl}$ . The analytically pure materials of **1c** were obtained by vapor diffusion of pentane or diethyl ether into a THF solution of **1c** at  $-20^\circ\text{C}$  for 2–4 days. Yield: 87% (3.73 g). X-ray quality single crystals of **1c** were chosen from the crystallization described above for structural determination.  $^1\text{H}$  NMR (400 MHz,  $d^8$ -THF, ppm) (Figure S9):  $\delta$  7.91 (Ar-H, 1H, bs), 7.77 (Ar-H, 4H, bs).  $^{13}\text{C}\{^1\text{H}\}$  NMR (100.52 MHz,  $d^8$ -THF, ppm) (Figure S10):  $\delta$  484.6 ( $\mu_6\text{-C}$ ), 229.1 (CO), 136.4 (Ar, JP-C = 3.3 Hz), 135.7 (Ar, JP-C = 10.0 Hz), 131.4 (Ar, JP-C = 13.3 Hz), 119.5 (Ar, JP-C = 89.5 Hz).  $^{31}\text{P}\{^1\text{H}\}$  NMR (161.83 MHz,  $d^8$ -THF, ppm) (Figure S11):  $\delta$  23.0. UV/vis in nm ( $\epsilon = \text{L mol}^{-1} \text{cm}^{-1}$ ) (Figure S12): 520 (4430). IR (solid state) (Figure S13): 1937, 1768  $\text{cm}^{-1}$ . Anal. Calcd for  $\text{C}_{65}\text{H}_{40}\text{O}_{16}\text{P}_2\text{Fe}_6$ : C, 52.96; H, 2.74. Found: C, 53.06; H, 2.81.

[ $\text{Fe}_6(\mu_6\text{-C})(\text{CO})_{16}$ ] $\cdot\text{THF}$  (**2**). A solution of **1a** (0.50 g, 0.53 mmol) in THF (15 mL) was combined with solid ferrocenium hexafluorophosphate (0.36 g, 1.1 mmol) at  $-78^\circ\text{C}$  under CO atmosphere. The resulting mixture was gradually warmed to room temperature and then stirred overnight. Insoluble materials were removed by filtration, and all volatiles were removed in vacuo. The ferrocene byproduct was thoroughly removed by multiple extractions with pentane (until clear), followed by extraction of the desired cluster into toluene. The reaction mixture was then purified through a pipet column packed with BioBeads (3–4 cm height), and then again through a second pipet column packed with  $\text{C}_{18}$  silica (3–4 cm height). All volatiles were then removed in vacuo to give the analytically pure material of **2** as a brick-red powder. Yield: 0.30 g (61%). UV/vis in nm ( $\epsilon = \text{L mol}^{-1} \text{cm}^{-1}$ ) (Figure S14): 472 (1700), 820 (100). IR (solid state) (Figure S15): 1965  $\text{cm}^{-1}$ . Anal. Calcd for  $\text{C}_{23}\text{H}_8\text{O}_{19}\text{Fe}_6$ : C, 29.92; H, 0.87. Found: C, 29.38; H, 1.18.

[ $\text{Fe}_5(\mu_5\text{-C})(\text{CO})_{15}$ ] (**3**).<sup>22</sup> A slurry of **1a** (1.36 g, 1.38 mmol) or **1b** (1.44 g, 1.38 mmol) in toluene (400 mL) was layered with degassed 30 mM aqueous solution (250 mL) of  $\text{FeCl}_3\cdot 6\text{H}_2\text{O}$  at room temperature under inert atmosphere. The resulting mixture was vigorously stirred at room temperature for 12 h, and during this period the toluene layer turned black. Next, the toluene layer was carefully separated out from the aqueous layer, and subsequently passed through a medium-pore-size PYREX glass frit packed with a thick pad of Celite. All volatiles were then removed in vacuo. The crude, black shiny residue was washed with pentane (removing trace amounts of green  $\text{Fe}_3(\text{CO})_{12}$ ) to obtain a black microcrystalline material of **3**. Yield from **1a**: 63% (0.62 g). Yield from **1b**: 25% (0.24 g).  $^{13}\text{C}\{^1\text{H}\}$  NMR (100.5 MHz,  $d^6$ -benzene, ppm) (Figure S16):  $\delta$  212.2 (CO), 209.3 (CO). UV/vis in nm ( $\epsilon = \text{L mol}^{-1} \text{cm}^{-1}$ ) (Figure S17): 520 (5490), 780 (2710). IR (solid state) (Figure S18): 2015, 1975, 1945  $\text{cm}^{-1}$ . Anal. Calcd for  $\text{C}_{16}\text{O}_{15}\text{Fe}_5$ : C, 27.01. Found: C, 26.90.

( $\text{NMe}_4$ )<sub>2</sub>[ $\text{Fe}_5(\mu_5\text{-C})(\mu_2\text{-CO})(\text{CO})_{13}$ ] (**4**).<sup>22</sup> A precooled ( $-20^\circ\text{C}$ ) solution of **3** (0.5 g, 0.7 mmol) in THF (25 mL) was added to a second vessel containing solid  $\text{KC}_8$  (0.19 g, 1.4 mmol). The reaction mixture was stirred at room temperature for 2 h, and to this was added solid  $\text{NMe}_4\text{Cl}$  (0.16 g, 1.4 mmol). The resulting mixture was stirred for 12 h, and then the insoluble materials were removed by filtration; the volatiles were removed in vacuo. Crystalline material of **4** was obtained by vapor diffusion of pentane into a THF solution. Yield: 79% (0.46 g).  $^1\text{H}$  NMR (400 MHz,  $d^8$ -THF, ppm) (Figure S19):  $\delta$  3.20 ( $\text{CH}_3$ , bs).  $^{13}\text{C}\{^1\text{H}\}$  NMR (100.5 MHz,  $d^8$ -THF, ppm) (Figure S20):  $\delta$  478.3 ( $\mu_5\text{-C}$ ), 229.1 (CO), 227.4 (CO), 223.4 (CO), 221.4 (CO), 56.0 ( $\text{CH}_3$ ). UV/vis in nm ( $\epsilon = \text{L mol}^{-1} \text{cm}^{-1}$ ) (Figure S21):

460 (6440), 690 (2050). IR (solid state) (Figure S22): 1910, 1710  $\text{cm}^{-1}$ . Anal. Calcd for  $\text{C}_{23}\text{O}_{24}\text{O}_{14}\text{N}_2\text{Fe}_5$ : C, 33.22; H, 2.91; N, 3.37. Found: C, 31.99; H, 3.07; N, 3.15.

**Physical Measurements.** NMR spectra were recorded at ambient temperature on a Varian DirecDrive 400 MHz instrument, and chemical shifts are reported in  $\delta$  (ppm). For  $^1\text{H}$  and  $^{13}\text{C}\{^1\text{H}\}$  NMR spectra, the solvent resonance was used as an internal reference; for  $^{31}\text{P}\{^1\text{H}\}$  NMR spectra, 85%  $\text{H}_3\text{PO}_4$  was used as an external standard (0 ppm). IR spectra were recorded on a Bruker Alpha spectrometer equipped with a diamond ATR crystal. UV/vis absorption spectra were obtained using a Varian Cary 6000i spectrometer and 0.1 mM solutions in 1 cm path length quartz cuvettes. Elemental analyses were performed at Midwest Micro Lab, IN. The Raman spectra were recorded on solid samples using a Renishaw InVia microscope with a 514 nm  $\text{Ar}^+$  laser operated below 4 mW. Mössbauer spectra were collected on a model MS4 WRC low field spectrometer and on a LHe6T spectrometer (SEE Co.; Edina, MN). Both instruments were calibrated using  $\alpha$ -Fe foil at room temperature.

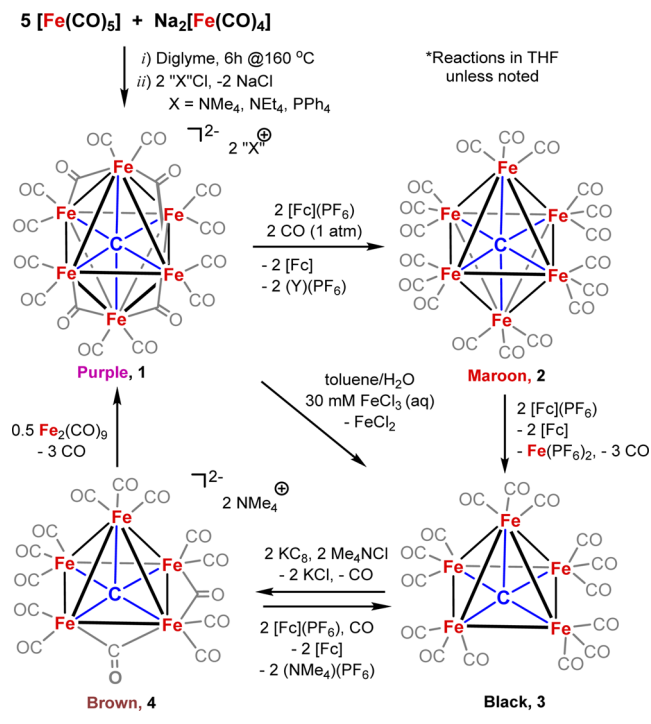
XP spectra were obtained using an X-ray photoelectron spectrometer (Kratos Axis Ultra) with a monochromated  $\text{Al K}\alpha$  X-ray source ( $h\nu = 1486.5 \text{ eV}$ ). The photoelectron takeoff angle was normal to the sample surface and  $45^\circ$  with respect to the X-ray beam. The pressure of the analysis chamber was sustained around  $2 \times 10^{-9}$  Torr during measurement. All spectra were obtained with a dwell time of 1200 ms  $\times$  1 sweep (Si atom), 3000 ms  $\times$  1 sweep (C atom), 1200 ms  $\times$  1 sweep (Br atom), 3000  $\times$  1 sweep (Al atom), and 1800  $\times$  1 sweep (Ti atom). A  $300 \times 700 \mu\text{m}^2$  spot and 20 eV of pass energy with resolution of 0.025 eV (Si atom) and 0.1 eV (C, Br, Al, and Ti atom) were used for the XPS measurement. The obtained spectra were analyzed by the Casa XPS software (version 2.3.15, Casa Software Ltd.) using 70% Gaussian and 30% Lorentzian function after subtraction of Tougaard background.

**X-ray Diffraction Data Collection and Crystal Structure Refinement.** The diffraction data for **1a**, **1b**, and **4** were collected on either an Agilent Technologies SuperNova Dual Source diffractometer or a Nonius Kappa CCD diffractometer using a Bruker AXS Apex II detector. The data for **1c** and **3** were collected on a Rigaku AFC12 diffractometer with a Saturn 724+ CCD, all using a graphite monochromator with  $\text{Mo K}\alpha$  radiation. Low temperatures were maintained using an Oxford Cryostream low temperature device. Data reductions were performed using either Agilent Technologies CrysAlisPro V 1.171.37.3<sup>30</sup> or Rigaku Crystal Clear version 1.40.2.<sup>31,32</sup> The structure was solved by direct methods using SIR97<sup>33</sup> and refined by full-matrix least-squares on  $F^2$  with anisotropic displacement parameters for the non-H atoms using SHELXL-2013.<sup>34</sup> Structure analysis was aided by use of the programs PLATON98<sup>35</sup> and WinGX.<sup>36</sup> The hydrogen atoms on carbon were calculated in ideal positions with isotropic displacement parameters set to  $1.2 \times U_{\text{eq}}$  of the attached atom ( $1.5 \times U_{\text{eq}}$  for methyl hydrogen atoms). Details of crystal data, data collection, and structure refinement are listed in Table S1. Experimental details and full thermal ellipsoid plots of **1a–c**, **3**, and **4** including counterions are given in the Supporting Information.

## RESULTS AND DISCUSSION

**Synthesis.** The violet cluster [ $\text{Fe}_6(\mu_6\text{-C})(\text{CO})_{16}$ ] $^{2-}$  was originally isolated as a decomposition product of the heterometallic anion [ $\text{MnFe}_2(\text{CO})_{12}$ ] $^-$  by Churchill.<sup>20</sup> We prepared this cluster according to an alternate report by the stoichiometric (in iron) reduction of 5 equiv of [ $\text{Fe}(\text{CO})_5$ ] with  $\text{Na}_2[\text{Fe}(\text{CO})_4]$  in diglyme at  $160^\circ\text{C}$  for 6 h (Scheme 1).<sup>22</sup> This procedure generated a violet solution of  $\text{Na}_2[\text{Fe}_6(\mu_6\text{-C})(\text{CO})_{16}]$ . Cation exchange with  $\text{NMe}_4\text{Cl}$ ,  $\text{NEt}_4\text{Cl}$ , or  $\text{PPh}_4\text{Cl}$  afforded X-ray quality crystals of ( $\text{Y}$ )<sub>2</sub>[ $\text{Fe}_6(\mu_6\text{-C})(\mu_2\text{-CO})_4(\text{CO})_{12}$ ] ( $\text{Y} = \text{NMe}_4$ ,  $\text{NEt}_4$ ,  $\text{PPh}_4$ ; **1a–c**) on multigram scale and in good yields (50–90%). One type of oxidation of **1** has been reported: reaction with  $\text{FeCl}_3$  in aqueous HCl results in oxidative elimination of an  $\{\text{Fe}(\text{CO})\text{Cl}_2\}$  unit, affording the

**Scheme 1. Synthesis of the Starting  $[\text{Fe}_6]^{2-}$  Cluster **1** (Top Left), Its Neutral Congener  $[\text{Fe}_6]^0$  (**2**, Top Right), and the Closed Synthetic Loop Including the Crystallographically Defined Five-Iron Clusters  $[\text{Fe}_5]^n$  ( $n = 0$  or  $2-$ ), Shown at Bottom**



five-iron cluster  $[\text{Fe}_5(\mu_5\text{-C})(\text{CO})_{15}]$  (**3**) in low yields (<30%).<sup>22</sup> However, there were no reports regarding the use of an outer-sphere redox agent with the  $[\text{Fe}_6]^{2-}$  cluster,<sup>37</sup> and we found no reports regarding the preparation of oxidized  $[\text{Fe}_6]^0$  species. In the present case, an outer-sphere oxidation route was used: reaction of **1** with 2 equiv of  $[\text{Fc}](\text{PF}_6)$  under an inert atmosphere leads to the isolation of a mixture of neutral species, including the carbonyl clusters  $[\text{Fe}_2(\text{CO})_9]$  (yellow),  $[\text{Fe}_3(\text{CO})_9]$  (green), the carbide-cluster  $[\text{Fe}_5(\mu_5\text{-C})(\text{CO})_{15}]$  (**3**), and the target  $[\text{Fe}_6]$  cluster (eventually identified as  $[\text{Fe}_6(\mu_6\text{-C})(\text{CO})_{18}]$  (**2**)). However, the same reaction under CO atmosphere cleanly affords the red solid of **2** in good yield. To ensure purity, the complex was sequentially purified through cross-linked polystyrene beads (BioBeads,

Biorad) and  $\text{C}_{18}$ -silica gel. The complex is not stable upon exposure to underivatized silica or alumina gel, or in coordinating solvents, or under ambient light conditions. Such instability is likely the reason for the lack of previous reports on this complex, despite significant work on the stable clusters **1a**, **3**, and **4**.

To further establish the identity of **2**, in relation to its known  $[\text{Fe}_6]$  and  $[\text{Fe}_5]$  relatives, we performed synthetic interconversions according to Scheme 1. Mild oxidation of **2** with 2 more equiv of  $[\text{Fc}](\text{PF}_6)$  under dilute conditions smoothly afforded  $[\text{Fe}_5(\mu_5\text{-C})(\text{CO})_{15}]$  (**3**, determined by single-crystal X-ray; Figure 2, left). Subsequent two-electron reduction of **3** with 2 equiv of  $\text{KC}_8$ , followed by  $\text{K} \rightarrow \text{NMe}_4$  cation-exchange, smoothly afforded the brown  $[\text{Fe}_5]^{2-}$  species  $(\text{NMe}_4)_2[\text{Fe}_5(\mu_5\text{-C})(\mu_2\text{-CO})(\text{CO})_{12}]$  (**4**). Notably, this reaction can be reversed by facile two-electron oxidation of **4** under CO atmosphere with  $[\text{Fc}](\text{PF}_6)$  to regenerate **3** in quantitative yield. Finally, to complete the synthetic loop, the  $[\text{Fe}_5]^{2-}$  cluster **4** can be utilized to reform the parent  $[\text{Fe}_6]^{2-}$  cluster **1** by "capping" it with 0.5 equiv of  $[\text{Fe}_2(\text{CO})_9]$  in THF at ambient temperature, which cleanly regenerates **1** in quantitative yield.<sup>22</sup>

**X-ray Structures. Six Iron Clusters.**  $(\text{Y})_2[\text{Fe}_6(\mu_6\text{-C})(\mu_2\text{-CO})_4(\text{CO})_{12}]$  ( $\text{Y} = \text{NMe}_4, \text{NEt}_4, \text{PPh}_4$ ; **1a–c**). The original (1971) report of the low-resolution, room-temperature X-ray structure of **1a** by Churchill and co-workers did not satisfactorily describe the connectivity or bond metrics of the bridging carbonyls.<sup>20,21</sup> In a recent report, a phase transition for **1a** was observed between 200 K and room temperature, in which one of the bridging carbonyls alternates between two iron atoms, and as a consequence attains lower symmetry at higher temperatures.<sup>38</sup> To circumvent these limitations and ambiguities, the precise low temperature structures of **1a–c** ( $\text{Y} = \text{NMe}_4, \text{NEt}_4, \text{PPh}_4$ ) were determined (Figure 1, Figures S23–S25). The structure of **1c** ( $\text{Y} = \text{PPh}_4$ ) provides both a higher resolution and a higher symmetry structure, without the complications of a phase transition as found for **1a** (Tables S1 and S2). Table 1 lists the pertinent interatomic parameters for comparison. All of the anions retain the same molecular formula and are mostly isostructural, but differ in the connectivity of their (semi)bridging carbonyls.

Cluster **1a** crystallizes in space group  $P2_1$  with two molecules in the asymmetric unit. Clusters **1b** and **1c** crystallize in orthorhombic and monoclinic space groups  $P4_2/\text{nnm}$  and  $P2_1$ , respectively, and each structure has just one anion per asymmetric unit. The high crystallographic symmetry of **1b**,

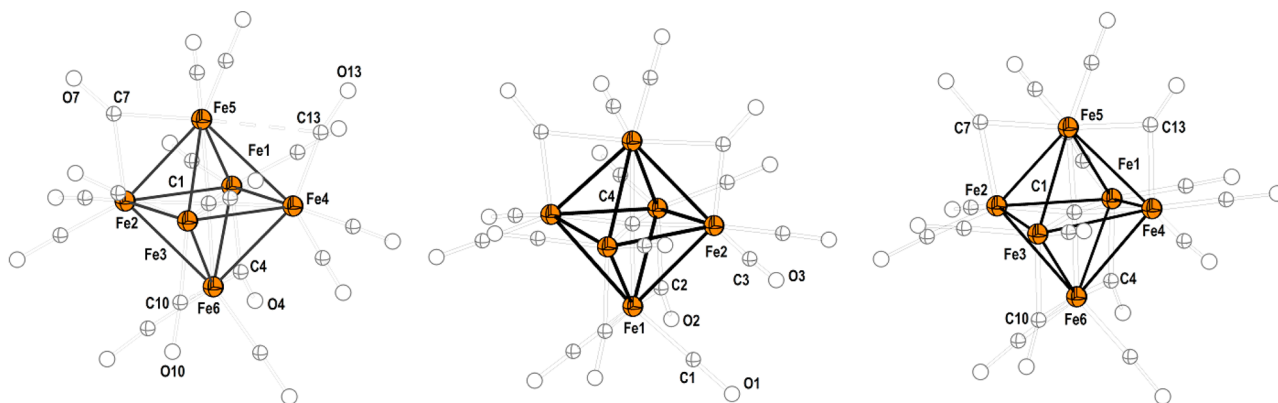


**Figure 1.** Molecular structures (isotropic view) of the anions in the crystal structures of **1a–c** ( $\text{Y} = \text{NMe}_4, \text{NEt}_4, \text{PPh}_4$ ; from left to right, respectively); counter-cations and solvents are omitted for clarity. Full thermal ellipsoid plots are shown in Figures S23–25.

Table 1. X-ray Diffraction Experimental Details for 1a–c, 3, and 4

	1a	1b	1c	3	4
formula	C <sub>29</sub> H <sub>32</sub> Fe <sub>6</sub> N <sub>2</sub> O <sub>17</sub>	C <sub>33</sub> H <sub>40</sub> Fe <sub>6</sub> N <sub>2</sub> O <sub>16</sub>	C <sub>63</sub> H <sub>40</sub> Fe <sub>6</sub> O <sub>16</sub> P <sub>2</sub>	C <sub>16</sub> Fe <sub>5</sub> O <sub>15</sub>	C <sub>23</sub> H <sub>24</sub> Fe <sub>3</sub> N <sub>2</sub> O <sub>14</sub>
fw	1015.66	1055.77	1474.01	711.41	831.69
T (K)	133(2)	133(2)	100(2)	100(2)	100(2)
λ (Å)	0.71073	0.71073	0.71073	0.71073	0.71073
a (Å)	11.4065(3)	11.7157(4)	11.0889(16)	16.599(16)	19.5579(13)
b (Å)	15.6419(5)	11.7157(4)	14.517(2)	8.8900(19)	10.8967(10)
c (Å)	21.1122 (7)	16.8663(6)	18.902(3)	29.696(7)	28.9033(16)
α (deg)	90	90	90	90	90
β (deg)	91.210(4)	90	101.209(4)	105.337(8)	96.463(6)
γ (deg)	90	90	90	90	90
V (Å <sup>3</sup> )	3766.0(2)	2315.03(18)	2984.8(8)	4225.9(16)	6120.6(8)
space group	P2 <sub>1</sub>	P42/nmm	P2 <sub>1</sub>	C2/c	C2/c
Z	4	2	2	8	8
D <sub>calcd</sub> (mg/cm <sup>3</sup> )	1.791	1.515	1.640	2.236	1.805
μ (mm <sup>-1</sup> )	2.325	1.923	1.545	3.431	19.173
GOF on F <sup>2</sup>	1.054	1.339	1.067	1.155	1.054
R <sub>1</sub> (I > 2σ(I))	0.0352	0.0345	0.0363	0.0660	0.1104
wR <sub>2</sub> <sup>a</sup> (all)	0.0773	0.1087	0.0924	0.1370	0.3320
R <sub>int</sub>	0.0372	0.0532	0.033	0.100	0.1599
N <sub>ref</sub> (all)	41422	47922	33022	25556	26965
N <sub>ref</sub> (I > 2σ(I))	17007	1430	10481	3716	6220

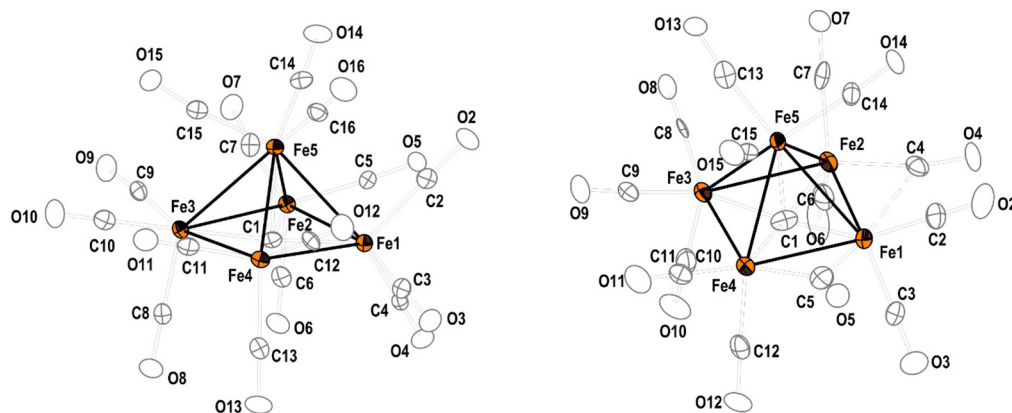
$$^a R_1 = \sum \|F_o\| - |F_c| / \sum |F_o|; wR_2 = \{ \sum [w(F_o^2 - F_c^2)_2] / \sum [w(F_o^2)] \}^{1/2}.$$

Table 2. Selected Bond Distances for the 1a–c and DFT Optimized Distances (I<sub>DFT</sub>) Reported in This Work, As Well As the Published Structure (I<sub>pub</sub>)

bonds	1a (NMe <sub>4</sub> )	1b (NEt <sub>4</sub> )	1c (PPh <sub>4</sub> )	I <sub>pub</sub> <sup>21</sup>	I <sub>DFT</sub>
Fe1–C1/C4	1.896(5), 1.877(5)	1.8743(7)	1.878(5)	1.963(36), 1.968(38)	1.8697
Fe2–C1/C4	1.876(5), 1.890(5)	1.8838(5)	1.874(5)	1.888(35), 1.884(38)	1.8692
Fe3–C1	1.897(5), 1.902(5)		1.886(5)	1.862(36), 1.821(38)	1.8684
Fe4–C1	1.908(5), 1.906(5)		1.898(5)	1.888(35), 1.884(38)	1.8679
Fe5–C1	1.876(5), 1.869(5)		1.897(4)	1.834(36), 1.805(38)	1.8771
Fe6–C1	1.885(5), 1.885(5)		1.881(4)	1.907(36), 1.949(38)	1.8775
Fe1/Fe2–C4/C2	1.948(5), 1.959(5)	1.869(4)	1.895(4)	1.969(60), 1.905(63)	1.8219
Fe6/Fe1–C4/C2	1.947(5), 1.960(5)	2.101(4)	2.064(4)	2.326(61), 2.005(63)	2.0439
Fe2–C7	1.966(5), 1.946(5)		1.878(4)	1.780(43), 1.791(60)	1.8216
Fe5–C7	1.965(6), 1.953(6)		2.136(4)	2.163(43), 2.213(60)	2.0459
Fe3–C10	1.804(6), 1.799(6)		1.882(4)	2.222(10), 2.330(2)	1.8197
Fe6–C10	2.707(0), 2.654(4)		2.077(4)	2.720(3), 2.583(2)	2.0494
Fe4–C13	1.809(6), 1.800(6)		1.899(4)	1.780(43), 1.791(60)	1.8201
Fe5–C13	2.692(4), 2.709(0)		2.036(4)	2.163(43), 2.213(60)	2.0482
Fe1–Fe2	2.700(1), 2.702(1)	2.5955(7)	2.6561(9)	2.706(9), 2.688(9)	2.6478
Fe1–Fe4/Fe2#1	2.684(1), 2.668(1)	2.7180(7)	2.6771(9)	2.706(9), 2.688(9)	2.6448
Fe1–Fe5	2.711(1), 2.679(1)		2.7559(9)	2.662(11), 2.725(10)	2.6926
Fe1–Fe6	2.577(1), 2.584(1)		2.5964(8)	2.609(10), 2.553(10)	2.601
Fe2–Fe3/Fe2#1	2.671(1), 2.680(1)	2.6670(8)	2.6721(9)	2.699(9), 2.654(9)	2.6428
Fe2–Fe5	2.583(1), 2.574(1)		2.6050(8)	2.632(10), 2.621(9)	2.5994
Fe2–Fe6	2.682(1), 2.705(1)		2.6663(8)	2.682(9), 2.695(9)	2.6945
Fe3–Fe4	2.659(1), 2.661(1)		2.6663(9)	2.699(9), 2.654(9)	2.6429
Fe3–Fe5	2.634(1), 2.662(1)		2.7139(9)	2.682(11), 2.646(10)	2.7001
Fe3–Fe6	2.758(1), 2.729(1)		2.5975(9)	2.743(10), 2.729(10)	2.6007
Fe4–Fe5	2.745(1), 2.750(1)		2.5795(8)	2.632(10), 2.621(9)	2.6012
Fe4–Fe6	2.660(1), 2.647(1)		2.8186(8)	2.682(9), 2.695(9)	2.698
Fe1···Fe3/Fe2···Fe2#1	3.792(5), 3.778(5)	3.764(0)	3.759(3)	3.779(0), 3.787(0)	3.7356
Fe2···Fe4	3.784(5), 3.796(0)		3.764(2)	3.788(4), 3.829(4)	3.7346
Fe5···Fe6/Fe1···Fe1#1	3.755(5), 3.754(5)	3.749(0)	3.777(2)	3.752(3), 3.739(6)	3.7546

in particular, mandates just two distinct Fe sites. For 1a–c, the cluster exhibits an octahedral μ<sub>6</sub>-carbido ligand at its center that supports the tightly knit network of Fe–C and Fe–Fe

bonds. The μ<sub>6</sub>-central carbide atom encapsulated by six equidistant iron atoms adopts a nearly octahedral geometry. The distances between carbide and iron atoms in 1a–c reside



**Figure 2.** Thermal ellipsoid plots (30% probability) of the molecular structures of the  $[\text{Fe}_5]^0$  cluster **3** (left) and the  $[\text{Fe}_5]^{2-}$  cluster **4** (right); counter-cations and solvents are omitted for clarity. Full thermal ellipsoid plots are shown in [Figures S26 and S27](#).

in the narrow range of 1.87–1.91 Å, whereas the original X-ray structure **1<sub>pub-1</sub>** exhibits a much broader range of distances between 1.80 and 1.97 Å. In the room-temperature structure,<sup>21</sup> the Fe ions with the longest Fe–C<sub>carbide</sub> bond appear to occupy positions trans from one another, thus revealing a pseudoaxial configuration about the carbide center. In contrast, all of the structures determined at low temperature (**1a–c**) exhibit a more uniform distribution of Fe–C<sub>carbide</sub> distances, indicating a more strictly octahedral arrangement of Fe ions about the central carbide. The primary difference within the set of matched anions involves the extent of bridging or semibridging carbonyls. For example, in cluster **1a** (NMe<sub>4</sub> salt), there are two semibridging carbonyls [e.g., Fe–C(O) = 1.799(6), 2.654(4) Å]. In clusters **1b** and **1c**, all four bridging carbonyls are more symmetric [e.g., **1b**, Fe–C(O) = 1.869(4), 2.101(4) Å].

Cluster **1b** has the highest symmetry, including two crystallographically distinct Fe sites. The Fe2 ion of **1b** represents four “equatorial” Fe sites, and exhibits an Fe–C<sub>carbide</sub> distance of 1.8838(5) Å. In contrast, the two “axial” Fe1 sites reside slightly closer to the carbide (Fe–C1 = 1.8743(7) Å). Considering only the carbide and carbonyl groups as ligands, the axial Fe1 sites in **1b** display a distorted trigonal bipyramidal geometry with two terminal and bridging carbonyls, and one bond to the central carbide. In this limited sense, the Fe1 ions are five-coordinate, with a total of 7 contributed e<sup>−</sup> donors: two terminal CO (2 e<sup>−</sup> each), two bridging CO (1 e<sup>−</sup> each), and one-half of a carbide 2p<sub>z</sub> (1 e<sup>−</sup>). In contrast, the equatorial Fe2 sites have trigonal pyramidal geometry, consisting of donors that collectively donate 6 e<sup>−</sup> to the metal: two terminal CO (2 e<sup>−</sup> each), one bridging CO (1 e<sup>−</sup> each), and one-half of a carbide 2p<sub>x/y</sub> (1 e<sup>−</sup>).

On the basis of the assignment of an axially oriented system about the central carbide, there are two types of Fe–Fe bond found in the cluster. The adjacent Fe–Fe bonds between the equatorial sites are in the range of 2.57–2.76 Å [2.6670(8) Å in **1b**], whereas the “diagonal” Fe–Fe bonds between Fe<sub>ax</sub> and Fe<sub>eq</sub> are slightly longer [2.7180(7) Å in **1b**]. Closer inspection of the structure reveals that each of the longer, “diagonal” Fe<sub>ax</sub>–Fe<sub>eq</sub> interactions are supported by a bridging CO unit, whereas the shorter Fe<sub>eq</sub>–Fe<sub>eq</sub> interactions are not. All of the Fe–Fe contacts in **1a–c** are longer than the Fe–Fe distances in metallic iron (2.48 Å)<sup>39</sup> or the sum of the covalent radii of two iron atoms (2.80 Å).<sup>40</sup> The Fe–Fe distances observed in these clusters are comparable to those of the  $[\text{Fe}_3(\text{CO})_{11}]^-$  anion

(2.60 Å).<sup>41</sup> Interestingly, they are slightly shorter than in  $[\text{Fe}_2(\text{CO})_8]^{2-}$  with organic cations (2.78–2.84 Å).<sup>42–44</sup>

**Five-Iron Clusters.**  $[\text{Fe}_5(\mu_5\text{-C})(\text{CO})_{15}]$  (**3**). The solid-state, room-temperature X-ray structure of **3** was reported.<sup>19</sup> In this work, we collected the low temperature data to confirm the connectivity of the atoms within the cluster. The isotropic view of the molecular structure of **3** is shown in [Figure 2](#) (full anisotropic thermal ellipsoid plot, [Figure S26](#)). Upon first inspection, the only considerable change in bond parameters noted in **3** as compared to the reported structure is a dramatic elongation (~0.2 Å) along the axis of the axial Fe5 ion ([Table 3](#)). This ion is 1.948(7) Å from the interstitial carbide at low

**Table 3.** Selected Bond Distances for **3** and **4** Reported in This Work, As Well as the Two Previously Published Structures Determined at Room Temperature

bonds	<b>3</b>	<b>3</b> <sub>RT</sub> <sup>19</sup>	<b>4</b>	<b>4</b> <sub>RT-NBu4</sub> <sup>45</sup>
Fe1–C1	1.875(8)	1.90(3)	1.882(13)	1.87(2)
Fe2–C1	1.897(7)	1.96(3)	1.866(14)	1.88(2)
Fe3–C1	1.865(8)	1.89(3)	1.853(13)	1.84(2)
Fe4–C1	1.893(7)	1.88(3)	1.862(14)	1.87(2)
Fe5–C1	1.948(7)	1.76(4)	1.993(13)	2.00(1)
Fe1–Fe2	2.6331(15)	2.675(6)	2.657(3)	2.597(4)
Fe1–Fe4	2.6496(15)	2.667(7)	2.506(3)	2.553(3)
Fe1–Fe5	2.6557(16)	2.650(6)	2.637(3)	2.597(4)
Fe2–Fe3	2.6703(15)	2.652(7)	2.651(3)	2.680(4)
Fe2–Fe5	2.5869(15)	2.600(7)	2.579(3)	2.591(2)
Fe3–Fe4	2.6780(15)	2.636(7)	2.692(3)	2.670(4)
Fe3–Fe5	2.6466(16)	2.666(7)	2.594(3)	2.590(2)
Fe4–Fe5	2.5997(14)	2.587(6)	2.607(3)	2.616(4)
Fe1–C4			2.532(0)	2.28(2)
Fe2–C4			1.813(14)	1.85(2)
Fe1–C5			1.990(16)	2.15(2)
Fe4–C5			1.904(15)	1.82(2)

temperature, as compared to the corresponding Fe–C<sub>carbide</sub> distance of 1.76(4) Å at room temperature. Interestingly, closer inspection of the equatorial Fe–C<sub>carbide</sub> distances reveals that they are anticorrelated with this trend: the longer Fe<sub>ax</sub>–C<sub>carbide</sub> distance of 1.948(7) Å found at low temperature goes along with comparatively short Fe<sub>eq</sub>–C<sub>carbide</sub> distances (avg = 1.883 Å, max = 1.897(7) Å), whereas the shorter Fe<sub>ax</sub>–C<sub>carbide</sub> distance of 1.76(4) Å found at room temperature is accompanied by generally longer Fe<sub>eq</sub>–C<sub>carbide</sub> distances (avg = 1.908 Å, max =

1.96(3)). This reflects the dynamic nature and structural preferences of the iron–carbide bonding motif.

(NMe<sub>4</sub>)<sub>2</sub>[Fe<sub>5</sub>(μ<sub>5</sub>-C)(μ<sub>2</sub>-CO)(CO)<sub>13</sub>] (**4**). As noted above regarding modulating the counter cations in clusters **1a–c**, the coordination mode of metal carbonyls swings between semibridging and bridging, which directly affects the electronics at the particular metal sites. The cluster type of [Fe<sub>5</sub>]<sup>2-</sup> has been known for several years, and used as a potential precursor for heterometallic cluster synthesis.<sup>22</sup> The reported cluster was prepared as [Fe<sub>5</sub>(μ<sub>5</sub>-C)(μ<sub>2</sub>-CO)<sub>2</sub>(CO)<sub>12</sub>]<sup>2-</sup> with two disordered NBu<sub>4</sub> cations in the structure based on data collected at room temperature.<sup>45</sup> To obtain more precise structural information, we reformulated the cluster as the NMe<sub>4</sub> salt and prepared single crystals of **4**. The refined molecular structure of the [Fe<sub>5</sub>]<sup>2-</sup> anion is shown in Figure 2; the full anisotropic thermal ellipsoid plots containing [Fe<sub>5</sub>]<sup>2-</sup> and NMe<sub>4</sub> ions can be found in Figure S27. The most notable difference between **4** and the reported cluster are the distances at the bridging carbonyl positions. For instance, one of the bridging iron–carbonyl distances in **4** is considerably longer (Fe1–C4 = 2.532 Å) than others (Fe2–C4 = 1.813 Å, Fe1–C5 = 1.990 Å, Fe4–C5 = 1.904 Å); however, more symmetrical bridging carbonyl distances are observed in the reported complex (Fe1–C4 = 2.274 Å, Fe2–C4 = 1.851 Å, Fe1–C5 = 2.149 Å, Fe4–C5 = 1.819 Å). Comparing cluster **4** with **3**, the anion's metal–metal bond distances are broadly dispersed across a range of ~0.2 Å (i.e., 2.506–2.692 Å), whereas the neutral cluster's Fe–Fe distances lie in a narrower range of ~0.1 Å (i.e., 2.590–2.680 Å). A similar trend is found in the Fe–C<sub>int</sub> distances (1.853–1.993 Å for **4**; 1.865–1.948 Å for **3**). In general, the metal–metal and metal–carbide distances of both **3** and **4** are comparable in **1a–c**.

**Infrared and Raman Characterization.** Figure 3 displays the solid-state IR spectra of [Fe<sub>6</sub>]<sup>2-</sup> (**1a**, left in violet) and

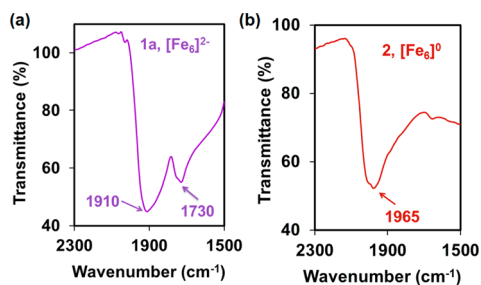


**Figure 3.** Solid-state IR spectra of **1a** and **2**. The feature at 1730 cm<sup>-1</sup> in the spectrum of **1a** indicates bridging CO ligands.

[Fe<sub>6</sub>]<sup>0</sup> (**2**, right in red). The terminal and bridging CO ligands in **1a** are evident in the absorption features at  $\nu_{\text{CO}} = 1910$  and 1730 cm<sup>-1</sup>, respectively. In contrast, the most prominent feature in the IR spectrum of **2** corresponds to a terminal  $\nu_{\text{CO}}$  feature at 1965 cm<sup>-1</sup>. This blue-shifted feature suggests an overall higher valence of the iron centers in the oxidized cluster, thus diminished  $d\pi(\text{Fe}) \rightarrow \pi^*(\text{CO})$  back-bonding. Additionally, the IR spectra of the crystallographically defined five-iron clusters **3** and **4** provide further analogy. While the dianion **4** does exhibit bridging carbonyls in its crystal structure and its solid-state IR spectrum ( $\nu_{\text{CO}} = 1710$  cm<sup>-1</sup>), the neutral cluster **3** does not. The lack of a bridging CO feature in the IR of **2** is consistent with either (a) a lack of bridging  $\nu_{\text{CO}}$  ligand(s) or (b) a lower symmetry structure with fewer experimentally

observable features (see DFT Calculations section for differentiation).

The Raman spectra of **1–4** provide insight into the symmetry of their structures. Dianion **1** exhibits several low energy features (150–600 cm<sup>-1</sup>) that are assigned to symmetric breathing modes that radiate from the central carbide. A DFT/Hessian calculation for **1** (vide infra, DFT section) indicates that these low-energy Raman modes arise from synchronized stretches among the Fe–(μ<sub>6</sub>-C), Fe–Fe, and bridging CO ligands (see DFT calculation results, Figure S29). The Raman spectrum of **1a** also exhibits a higher energy feature at 1320 cm<sup>-1</sup>, which is not readily assignable in the DFT calculation. This feature is likely another symmetric breathing mode that synchronizes the oscillations of the μ<sub>6</sub>-C–Fe<sub>6</sub> skeleton with the terminal CO ligands.

Interestingly, the Raman spectrum of **2** (Figure 4) exhibits only the higher energy resonance, observed at 1550 cm<sup>-1</sup> (μ<sub>6</sub>-

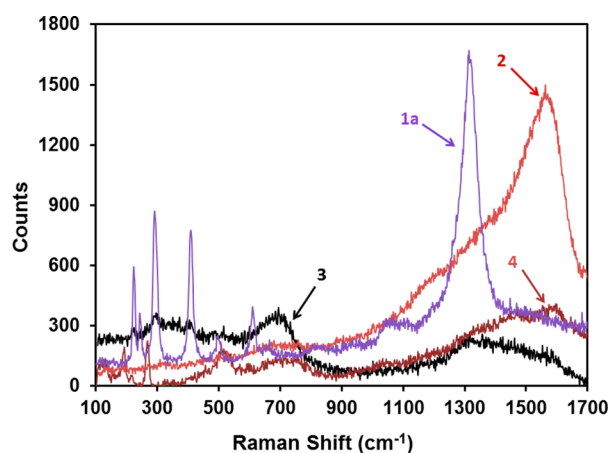


**Figure 4.** Solid-state Raman spectra of **1a**, **2**, **3**, and **4**;  $\lambda_{\text{ex}} = 532$  nm.

C–Fe<sub>6</sub> plus terminal CO); cluster **2** does not exhibit the lower energy features observed in **1a** that are associated with the symmetric breathing mode of the bridging CO ligands. As counter-examples, the Raman spectrum of **3** and **4** indicate a less symmetric (i.e., noncentrosymmetric) coordination environment about the interstitial carbide. Neither of these [Fe<sub>5</sub>]-type clusters exhibits any prominent absorption feature in the 150–2000 cm<sup>-1</sup> region (1700–2000 cm<sup>-1</sup> not shown) (Figure 4), consistent with the absence of symmetric breathing modes. As such, this indicates the retention of some form of a centrosymmetric (μ<sub>6</sub>-C)-[Fe<sub>6</sub>] core for **2**.

**XPS of 1 and 2.** To obtain further information regarding the formal or spectroscopic oxidation states contained in **1** and **2**, we collected their X-ray photoelectron spectra. Much like X-ray absorption spectroscopy (e.g., XAS K-edge), the binding energies observed in XPS correlate quite well to the average oxidation state(s) of the Fe clusters.<sup>46</sup> The comparative XP spectra (solid samples, room temperature, 1 × 10<sup>-9</sup> Torr) for **1a** and **2** are displayed in Figure 5. In our experiment, the XP spectrum for **1a** includes prominent core 2p (3/2, 1/2) features at 705.5 and 718.3 eV, slightly shifted from the values reported by Sosinsky and co-workers<sup>46</sup> (likely due to a different standardization procedure). In the case of **1**, the component fit of the spectrum was modeled using primarily one component, with the exception of a “trailing” feature on both the 2p<sub>3/2</sub> and the 2p<sub>1/2</sub> features; this trailing component is observed even in the case of mononuclear iron complexes that

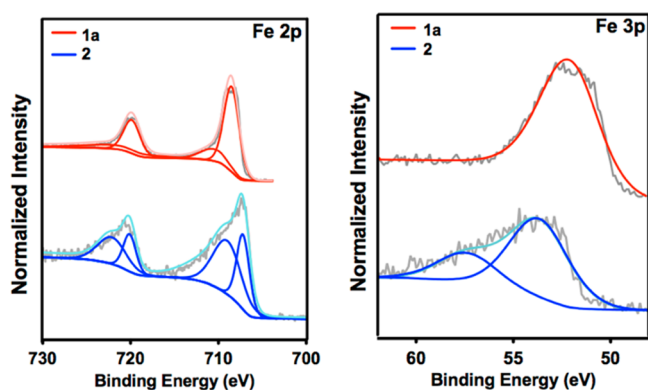


**Figure 5.** XP spectra for **1a** and **2** in the Fe 2p region (left) and Fe 3p region (right). Experimental conditions: solid samples, rt,  $1 \times 10^{-9}$  Torr, Al  $K\alpha$  X-ray source.

are unambiguously Fe(II), such as ferrocene.<sup>47</sup> Therefore, it can be concluded that the 2p spectrum for **1** is indicative of a single, delocalized oxidation state at room temperature. This is consistent with the reported room-temperature Mössbauer spectrum for **1**,<sup>46</sup> which was comprised of a single quadrupole doublet (vide infra). In contrast, the low temperature Mössbauer of **2** (vide infra) indicates two sets of irons with distinct coordination environments and/or oxidation states.

By comparison, the XP spectrum of **2** exhibits its core Fe 2p features at higher energy: 707.4 and 720.7 eV. This roughly +2 eV shift in ionization energy is consistent with an overall higher average Fe oxidation state in **2** versus **1**. Another interesting distinction between the 2p regions of **1** and **2** can be seen in the component fit for each cluster. In contrast to cluster **1**, the 2p region for **2** can only be modeled using two main components at {707.0/719.8 eV} and {708.8/721.9 eV} (plus the obligate trailing feature), in a ratio of 1:1.57 (low:high BE). This suggests fewer iron centers (possibly  $\sim 2/6$ ) in a higher oxidation state and more (possibly  $\sim 4/6$ ) in a lower oxidation state. Considering the evidence from the XP spectra of known clusters and complexes (see next paragraph), the formal charge on the two sets of irons in **2** could vary by as much as two units. Thus, the nominal oxidation state configurations for **2** could be  $(\text{Fe}^{2+})_2(\text{Fe}^0)_4$  or  $(\text{Fe}^{1+})_2(\text{Fe}^{0.5})_4$ , when considering the carbide as  $\text{C}^{4-}$ .

The reported XP spectra for the crystallographically defined five-iron clusters  $[\text{Fe}_5]^{2-}$  (**4**) and  $[\text{Fe}_5]^0$  (**3**) are insightful in this regard. In an early report, the reduced cluster **4** exhibited its Fe 2p edge feature at 707.9 eV, at higher energy as compared to the dianion **1a** (705.5 eV), due to the  $2^-$  charge distributed across fewer irons.<sup>46</sup> By comparison, the oxidized  $[\text{Fe}_5]^0$  cluster

**3** exhibited its 2p edge at 709.6 eV. The +1.5 eV shift observed for  $[\text{Fe}_5]^{2-} \rightarrow [\text{Fe}_5]^0$  (**4**  $\rightarrow$  **3**) is very similar to the +1.9 eV shift observed for  $[\text{Fe}_6]^{2-} \rightarrow [\text{Fe}_6]^0$  (**1**  $\rightarrow$  **2**). Overall, in this case, the +2 eV change in the 2p edge in going from **1**  $\rightarrow$  **2** likely reflects the analogous two-electron oxidation of the cluster.

Another indicator that has not been reported previously is the change in ionization energy of electrons closer to the valence shell, the 3p feature (Figure 5, right). Cluster **1** exhibits its 3p feature at 52.1 eV, whereas the corresponding feature in **2** is shifted to higher energy (53.7 eV). Similar to the trend for the 2p feature, this +1.5 eV shift to higher energy indicates an overall higher oxidation state in the oxidized cluster **2**. Overall, it is important to note that due to the “high” temperature of the experiment (298 K), only the average oxidation state across the cluster can be determined, and the precise distribution of oxidation states for a mixed-valence cluster cannot be resolved.

Two primary conclusions can be deduced from the XP spectra and corresponding contextual data (Table 4). First, it is clear that the oxidation from  $[\text{Fe}_6]^{2-} \rightarrow [\text{Fe}_6]^0$  (**1**  $\rightarrow$  **2**) is primarily iron-based. Second, the quantitative shift of about +2 eV supports a two-electron oxidation, as observed in the  $[\text{Fe}_5]^n$  case. Although the XP spectra provided tangible and direct evidence for the overall oxidation observed in **2**, further spectroscopic studies at low temperatures were required to investigate any possible mixed valence configuration of the ground state of **2**.

**Mössbauer Spectroscopy for 1 and 2.** A Mössbauer spectrum of the reduced cluster  $(\text{NMe}_4)_2[\text{Fe}_6(\mu_6\text{-C})(\mu_2\text{-CO})_4(\text{CO})_{12}]$  (**1a**) was collected at 5 K and 0.05 T ( $\gamma$ -rays parallel to the applied magnetic field). The spectrum (Figure 6) consisted of two partially overlapping quadrupole doublets. The solid red line is a simulation assuming the parameters delineated in Table 5. Sites 1 and 2 represented 2/6 and 4/6 of the spectral intensity, respectively. Within the context of the two axial Fe sites plus four equatorial Fe sites described in the X-ray section, site 1 corresponds to the two axial irons and site 2 to the four equatorial irons. The isomer shifts associated with both sites are similar, suggesting that the corresponding irons have the same or similar oxidation states. The Mössbauer spectrum of the same cluster at 295 K has been reported;<sup>38</sup>  $\Delta E_Q$  was 0.57  $\text{mm s}^{-1}$  and  $\delta$  was  $-0.004 \text{ mm s}^{-1}$  (we calibrated the reported value of  $\delta = 0.22 \text{ mm s}^{-1}$  vs sodium nitroprusside by subtracting 0.22  $\text{mm s}^{-1}$ ).<sup>48</sup> Minor differences observed between the  $\delta$  and  $\Delta E_Q$  values are probably due to temperature-dependent shifts.

A Mössbauer spectrum of the oxidized cluster **2** was collected at 5 K (Figure 6B) and at 30 K (Figure S28); the spectra were essentially indistinguishable. Both consisted of four quadrupole

**Table 4.** Summary of the IR, Raman, and XPS Properties of **1a–c**, **2**, **3**, and **4** from This Work and Previous Reports (As Indicated in the Table)

cluster	infrared ( $\text{cm}^{-1}$ )		Raman ( $\text{cm}^{-1}$ )		XPS Fe 2p (eV)		
	terminal CO	bridging CO	$\mu_6\text{-C-}[\text{Fe}_6]\text{-CO(bridging)}$	$\mu_6\text{-C-}[\text{Fe}_6]\text{-CO(terminal)}$	2p <sub>3/2</sub>	2p <sub>1/2</sub>	3p
<b>1a</b> $[\text{Fe}_6]^{2-}$	1910	1730	150–600	1320	705.5	718.3	52.1
<b>2</b> $[\text{Fe}_6]^0$	1965			1550	707.4	720.7	53.7
<b>3</b> $[\text{Fe}_5]^0$	2015				709.6 <sup>a</sup>	722.7 <sup>a</sup>	
	1975						
	1945						
<b>4</b> $[\text{Fe}_5]^{2-}$	1910	1710			707.9 <sup>a</sup>	720.4 <sup>a</sup>	

<sup>a</sup>Reference 46.

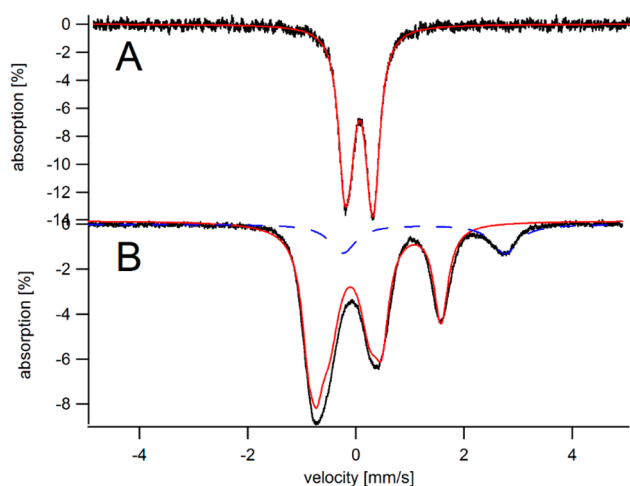


**Figure 6.** Mössbauer spectra of **1a** (A) and **2** (B) in frozen THF at 5 K and 0.05 T. Solid red lines are composite simulations using parameters given in Table 5. The paramagnetic impurity in cluster **2** (blue line in B) constitutes 16% of the iron in the sample.

doublets, with parameters as listed in Table 5. The parameters for sites 1 and 2 are similar to those of trigonal bipyramidal  $\text{Fe}(\text{CO})_5$  ( $\delta = -0.09 \text{ mm s}^{-1}$  and  $\Delta E_Q = 2.57 \text{ mm s}^{-1}$ ) and tetrahedral  $[\text{Fe}(\text{CO})_4]^{2-}$  ( $\delta = -0.18 \text{ mm s}^{-1}$  and  $\Delta E_Q = 0 \text{ mm s}^{-1}$ ).<sup>49</sup> Thus, the isomer shift values for sites 1 and 2 suggest iron oxidation states between 0 and  $-2$ . Site 4 was not simulated in Figures 6 or 7, as it was ascribed to adventitious iron.

To further investigate the magnetic properties of **2**, Mössbauer spectra were collected at 4.2 K with applied fields ranging from 0–6 T (Figure 7). Spectra were fitted assuming that the spin state of the oxidized cluster was either  $S = 0$  or  $S = 1$ . Site 4 was likely a paramagnetic contaminant,<sup>50,51</sup> so spectral intensity due to this site was ignored in the fitting. Simulations assumed two cluster sites, including one with  $\delta$  and  $\Delta E_Q$  values that were the average of those parameters for sites 1 and 2 (Figure 7, yellow line), and the other with  $\delta$  and  $\Delta E_Q$  values for site 3 (Figure 7, green line). The two sites represented 4/6 and 2/6 of the remaining spectral intensity, respectively. Simulations that assumed  $S = 0$  (Figure 7, red lines) fit the spectra acceptably well at all applied fields, whereas those that assumed  $S = 1$  did not. We conclude that the oxidized cluster is diamagnetic.

**DFT Calculations for 1 and 2.** To provide further insight into the electronic structure of **1**, as well as structural

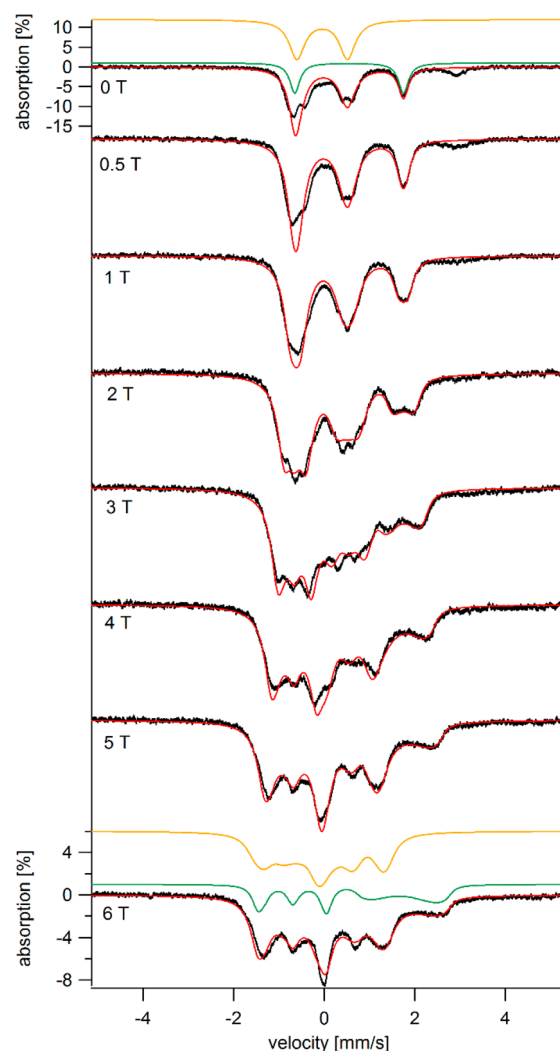


**Figure 7.** Variable field 4.2 K Mössbauer spectra for a frozen solution of **2** in toluene. Fields were applied perpendicular to the  $\gamma$  radiation. Red lines are composite simulations assuming parameters given in Table 5 and described in the text. The gold and green lines are simulations for the equatorial and axial irons, respectively.

possibilities for **2**, DFT calculations were pursued. To validate the calculation parameters, we first compared the X-ray structural parameters of **1** to the bond metrics derived from the DFT optimized structure of  $\mathbf{1}_{\text{DFT}}$  (B3PW91/G6-31). Figure 8 displays the geometry optimized structure of  $\mathbf{1}_{\text{DFT}}$ . Similar to

**Table 5.** Mössbauer and Parameters for **1a** and **2**

cluster and site	Mössbauer parameters				DFT charges	
	$\delta$ ( $\text{mm s}^{-1}$ )	$\Delta E_Q$ ( $\text{mm s}^{-1}$ )	$\Gamma$ ( $\text{mm s}^{-1}$ )	area (%)	Mulliken	
$(\text{NMe}_4)_2[\text{Fe}_6(\mu_6\text{-C})(\text{CO})_{16}]$ ( <b>1a</b> )						
site 1 (ax)	0.076	0.36	0.26	37	0.0377, 0.0376	
site 2 (eq)	0.064	0.57	0.27	63	0.449, 0.450, 0.449, 0.453	
carbide					-1.269	
$[\text{Fe}_6(\mu_6\text{-C})(\text{CO})_{18}]$ ( <b>2</b> )						
site 1 (eq)	-0.20	1.37	0.29	22	0.353, 0.374	
site 2 (eq)	-0.11	0.76	0.47	42	0.383, 0.428	
site 3 (axial)	0.42	2.30	0.32	30	0.465, 0.586	
site 4	1.2	2.8	0.58	16		
carbide					-1.045	

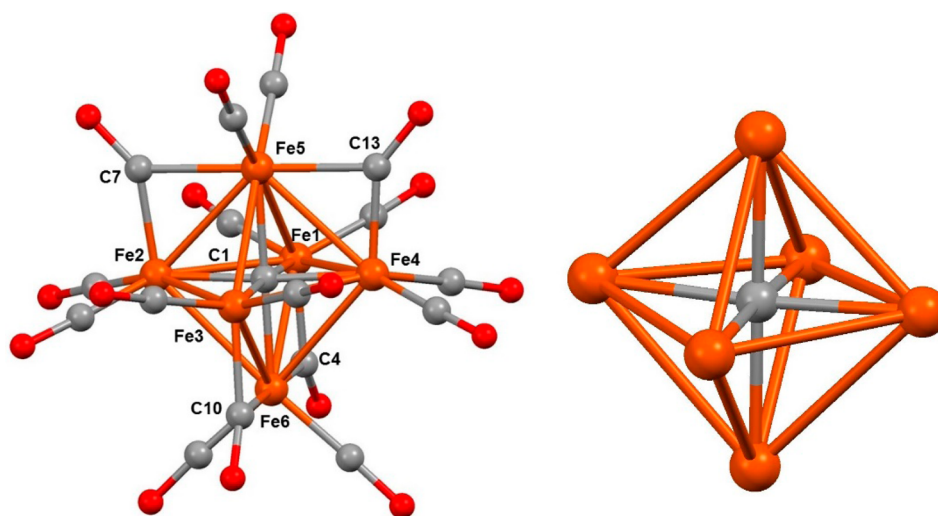


**Figure 8.** Molecular structure of the DFT-optimized structure for  $1_{\text{DFT}}$ : (left) complete view of the structure including CO ligands; (right) truncated view of the iron-carbide structure to highlight the  $[\text{Fe}_6(\text{C})]^{2-}$  core.

**Table 6. Summary and Comparisons of the Experimental (X-ray) and Calculated Averages for Fe–C<sub>int</sub>, Fe–C(O), and Fe–Fe Bond Lengths (Å) in 1a–c, 1<sub>pub</sub>, 1<sub>DFT</sub>, and 2<sub>DFT</sub>**

	$[\text{Fe}_6(\mu_6\text{-C})(\mu_2\text{-CO})_4(\text{CO})_{12}]^{2-}$					$[\text{Fe}_6(\mu_6\text{-C})(\text{CO})_{18}]$
	1a	1b	1c	1 <sub>pub</sub> <sup>21</sup>	1 <sub>DFT</sub> <sup>a</sup>	2 <sub>DFT</sub>
Fe–C(carbide) [all]	1.889(14)	1.879(6)	1.886(10)	1.888(53)	1.8716 ± 17	1.96 ± 4
Fe–C(carbide) [Ax]					1.87730 ± 14	2.016 ± 16
Fe–C(carbide) [Eq]					1.8688 ± 3	1.84 ± 3
Fe–C(O) [all]	2.101(357)	1.985(164)	1.983(105)	2.122(285)	1.81 ± 3	1.84 ± 2
Fe–Fe [all]	2.671(53)	2.660(62)	2.667(70)	2.671(44)	2.647 ± 11	2.76 ± 8
Fe–Fe [Ax–Eq]					2.648 ± 17	2.73 ± 4
Fe–Fe [Eq–Eq]					2.6446 ± 10	2.8 ± 2

<sup>a</sup>DFT values are presented as avg ± std dev across the multiple instances of that bond in the calculated cluster.

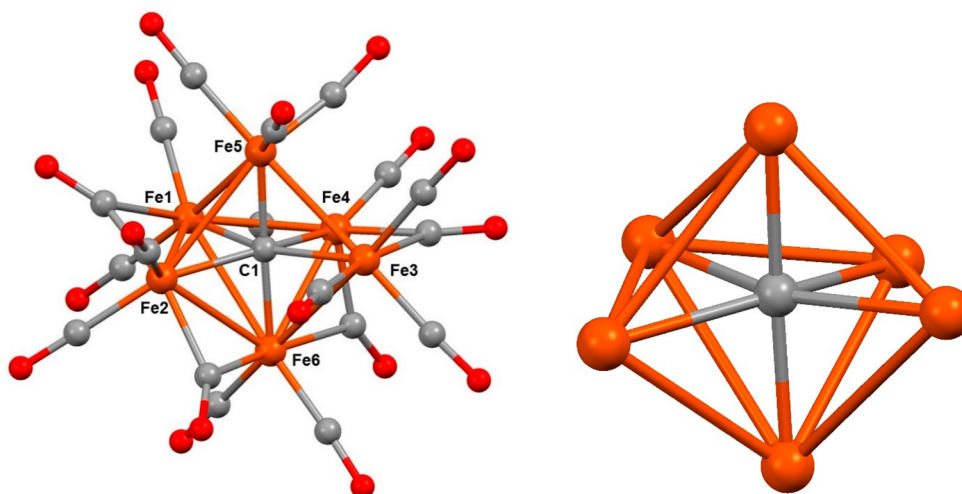


**Figure 9.** Molecular structure of the DFT-optimized structure for  $[\text{Fe}_6(\mu_6\text{-C})(\text{CO})_{18}]$  ( $2_{\text{DFT}}$ ): (left) complete view of the structure including CO ligands; (right) truncated view of the iron-carbide structure to highlight the  $[\text{Fe}_6(\text{C})]$  core.

the most symmetric experimental structure **1c**, the number of bridging COs (4) in  $1_{\text{DFT}}$  was minimized. As shown in the last column of **Table 2** (X-ray section) and above in the more concise **Table 6**, the DFT-optimized average distances for the Fe–C(carbide) bonds (1.872 Å) and Fe–Fe bonds (2.647 Å) are within the range of the experimentally determined bond distances. In contrast, the most clearly variable metric is the

average Fe–C(O) distance, which varies from 1.983–2.122 Å in the experimental data due to the range of bridging to semibridging to terminal carbonyls observed in the X-ray structures. The DFT calculated average Fe–C(O) bond for  $1_{\text{DFT}}$  (1.81 Å) is notably shorter than the shortest experimental distances in **1b** and **1c** (1.985 and 1.983 Å, respectively), which exhibit more symmetric bridging carbonyl ligands (unlike the

semibridging COs found in **1a** and **1<sub>pub</sub>**). Overall, one can conclude that the DFT calculated structure of **1<sub>DFT</sub>** accurately models the  $[\text{Fe}_6(\text{C})]$  core structure of **1a–c**, although some question remains regarding the predictive power of the calculation with respect to Fe–C(O) bond distances. Nonetheless, we conclude that the DFT calculation parameters are appropriate for predicting the core structure and electronic configuration for a given iron-carbido-carbonyl cluster to a first approximation. In this case, the given cluster is  $[\text{Fe}_6(\mu_6\text{-C})(\text{CO})_{18}]$  (**2**), for which we were unable to crystallographically determine its structure.

Thus, DFT computations were used to predict the structure of  $[\text{Fe}_6(\mu_6\text{-C})(\text{CO})_{18}]$  (**2**). In principle, this formulation could include six  $\{\text{Fe}(\text{CO})_3\}$  units capping the central carbide (only terminal COs). However, this general structure proved unstable: using severely restricted gradient perturbation parameters prevented the DFT system from converging. In contrast, looser constraints on geometry optimization revealed a very different core structure for **2** versus that for **1**. One face of the cluster was opened by breaking an equatorial Fe–Fe bond (Figure 9; new Fe...Fe distance, 3.589 Å), and the remaining equatorial Fe–Fe bonds shortened slightly ( $\text{Fe}_{\text{Eq}}\text{–Fe}_{\text{Eq}} = 2.451, 2.596, 2.604$  Å), while the axial  $\text{Fe}(\text{CO})_3$  units compressed ( $\text{Fe}\text{–C}_{\text{carbide}} = 1.817$  Å) as compared to the equatorial iron-tricarbonyl units ( $\text{Fe}\text{–C}_{\text{carbide}} = 1.981$  Å). The average Fe–C(O) distance for **2<sub>DFT</sub>** (1.84 Å) remained similar to that for **1<sub>DFT</sub>** ( $\text{Fe}\text{–C}(\text{O}) = 1.81$  Å).

Overall, this “open” structural motif is reminiscent of the open “butterfly” shape of the four-iron carbido cluster  $[\text{Fe}_4(\mu_4\text{-C})(\text{CO})_{13}]$ ,<sup>3,23</sup> wherein the four-coordinate carbide is exposed to the solvent on one face of the cluster. In this sense, **2** represents a hybrid of structural motifs borrowed from the six-iron, closed structure of the  $[\text{Fe}_6]^{2-}$  dianion (**1**), and the open structure of the four-iron cluster  $[\text{Fe}_4]^0$ . The five-iron clusters of intermediate nuclearity (both neutral and dianion) exhibit their open sites below the basal plane of the square pyramidal core structure (defined by the carbide and the four equatorial Fe centers). Perhaps most importantly, the symmetry of the calculated structure provides three chemically distinct iron sites, which is consistent with the three Fe sites observed in the Mössbauer spectrum of **2**.

To further substantiate the validity of the DFT calculations for **1** and **2**, we also used those calculations to predict IR spectra (Hessian calculation) for each cluster. The predicted IR spectrum for cluster **1<sub>DFT</sub>** (Figure S30, Table S4; scaling factor 0.9631)<sup>62</sup> includes two remarkably prominent and exclusive features: a single terminal feature at  $1891\text{ cm}^{-1}$  (cf., exp avg =  $1916\text{ cm}^{-1}$ , Figures S4, S8, and S13), and two less intense bridging CO features at  $1737$  and  $1721\text{ cm}^{-1}$  (cf., exp avg =  $1747\text{ cm}^{-1}$ ). The results are quite consistent with the experimental IR spectra for **1**. Regarding the less symmetric cluster **2<sub>DFT</sub>** (IR, Figure S31), a broader range of both terminal CO stretches ( $1958\text{–}1972\text{ cm}^{-1}$ ) and bridging CO stretches ( $1733\text{–}1808\text{ cm}^{-1}$ ) is observed, consistent with the broader experimental spectrum. Interestingly, the bridging CO features cannot be identified in the experimental spectrum for **2** (Figure S15), likely due to contributions from multiple yet weak oscillations.

## DISCUSSION

**Structure, Mössbauer, and DFT Interrelations.** Oxidized cluster **2** (or  $[\text{Fe}_6]^0$ ) was obtained from the dianion **1** by a two-electron oxidation. These two electrons were removed

from site 1 irons of the reduced cluster, forming the site 3 irons of the oxidized cluster. The 1:2 area ratio of site 1:site 2 in the reduced cluster suggests that site 1 represents axial irons and site 2 equatorial irons. The isomer shift of the site 3 doublet in the oxidized cluster was  $0.33\text{ mm s}^{-1}$  greater than that for site 1 of the reduced cluster, indicating a substantial oxidation. In contrast, the  $\delta$  values of sites 1 and 2 of the oxidized cluster were ca.  $0.2\text{ mm s}^{-1}$  lower than those of the reduced cluster. The simplest interpretation of the Mössbauer spectra of the reduced cluster is that all six irons of the reduced cluster have a formal oxidation state of +1/3. However, the decreased symmetry of the cluster and the DFT Mulliken charges suggest 2  $\text{Fe}^0$  (axial) and 4  $\text{Fe}^{+0.5}$  (equatorial) sites. In that case, the two electrons removed during oxidation of the dianion would come from the two axial  $\text{Fe}^0$  ions (which become the “site 3”  $\text{Fe}^{\text{II}}$ s in the oxidized cluster). This suggests that sites 1 and 2 become reduced from  $\text{Fe}^{+0.5}$  to  $\text{Fe}^0$  upon oxidation of the cluster (Figure 3). We conclude that the irons of the reduced cluster further disproportionate upon oxidation, with equatorial irons becoming reduced and axial irons becoming oxidized.

There is some precedence for individual irons of a carbonyl carbide Fe cluster becoming reduced when the cluster overall becomes oxidized. Sosinsky et al. reported that  $\delta$  values decline as the anionic charge on Fe carbonyl clusters increases;<sup>46</sup> for example, in the series  $[\text{Fe}_2(\text{CO})_9]^0$ ,  $[\text{Fe}_2(\text{CO})_8\text{H}]^-$ , and  $[\text{Fe}_2(\text{CO})_8]^{2-}$ ,  $\delta = 0.42, 0.33,$  and  $0.18\text{ mm s}^{-1}$ . However, trends involving  $\delta$  were opposite for several iron-carbido carbonyl clusters:  $[\text{Fe}_5\text{C}(\text{CO})_{15}]^0$  had lower  $\delta$  than did  $[\text{Fe}_5\text{C}(\text{CO})_{14}]^{2-}$  ( $0.20$  vs  $0.35\text{ mm s}^{-1}$ , respectively), which suggests that the iron framework in the neutral (oxidized) cluster is more electron rich than that in the dianion (reduced) cluster. These researchers suggested that the additional electron density was localized on the carbido carbon in the dianion, such that the irons in the dianion are more oxidized even though the overall cluster is more reduced.<sup>46</sup> They also suggested that the cluster distorts (similar to that seen in  $[\text{Fe}_4\text{C}(\text{CO})_{12}]^{2-}$  vs  $[\text{Fe}_4(\text{CO})_{13}]^0$ ) to alter the dihedral angle about carbon and Fe–C bond lengths.

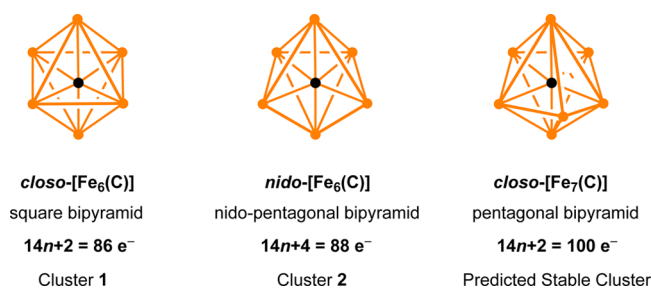
In the clusters that we have investigated, the average isomer shift of the four equatorial irons of the oxidized neutral cluster was lower than that of the reduced dianion cluster irons ( $-0.15\text{ mm s}^{-1}$  vs  $+0.07\text{ mm s}^{-1}$ ). This follows the same trend reported by Sosinsky, supporting the idea that the carbido carbon accepts a significant amount of the additional electron density associated with the reduced cluster. Upon oxidation, most electron density comes out of the two axial irons (and some out of the carbide). It is possible that the bonding of the equatorial irons to the carbido ion weakens such that these Fe centers are more easily reduced.

Lee and Peters have investigated a series of three monocarbonyl Fe complexes in which the Fe oxidation state is formally 0, +1, and +2.<sup>52</sup> Treatment of the complex in the most reduced state with  $\text{Me}_3\text{SiOTf}$  (trimethylsilyltrifluoromethanesulfonate) afforded an iron carbyne that included a  $\text{Fe}\equiv\text{C}\text{–O}\text{–SiMe}_3$  unit. Here, a strongly  $\pi$ -accepting Fischer-type carbyne ligand, in which the iron back-donates to the carbon, stabilized the  $\text{Fe}^0$  state rather than  $\text{Fe}^{\text{IV}}$ . These researchers regarded the carbyne as a  $\{\text{COSiMe}_3\}^+$  closed-shell cation, with one  $\sigma$  donor and two  $\pi$  acceptor orbitals at the carbon. The range of isomer shifts is compressed due to strong covalency. The isomer shifts of the  $\{\text{Fe}\text{–CO}\}^-$ ,  $\{\text{Fe}\text{–CO}\}$ , and  $\{\text{Fe}\text{–CO}\}^+$  moieties shift positive as the overall charge (and the relative Fe oxidation state) increases from  $\text{Fe}^0$  ( $\delta = 0.089\text{ mm}$

$s^{-1}$ ) to  $\text{Fe}^{\text{I}}$  ( $\delta = 0.21 \text{ mm s}^{-1}$ ) to  $\text{Fe}^{\text{II}}$  ( $\delta = 0.31 \text{ mm s}^{-1}$ ). The isomer shift of the related carbyne complex ( $\delta = 0.061 \text{ mm s}^{-1}$ ) is essentially the same as that for the equatorial Fe's of  $[\text{Fe}_6]_0$ , which rules out the  $\text{Fe}^{\text{IV}}$  designation and supports the  $\text{Fe}^0$  assignment. The isomer shift for  $d^8$  ( $\text{Fe}^0$ ) trigonal bipyramidal carbonyl complexes range from  $-0.09$  to  $-0.18 \text{ mm s}^{-1}$ .<sup>52</sup> Last, although the ligand environment is quite different, iron carbide nanoparticles exhibit Mössbauer spectra that include a doublet with  $\delta = 0.41 \text{ mm s}^{-1}$ ,  $\Delta E_{\text{Q}} = 1.06 \text{ mm s}^{-1}$  at  $7 \text{ K}$ ,<sup>9</sup> which is rather similar to the parameters of site 3.

**Cluster Electron-Counting Perspective.** Another lens through which to view and give context to the present results are the metalocluster electron counting rules, analogous to Wade's rules for carboranes.<sup>53</sup> Of particular use in this case are the "14n+2" rule for *closo* structures, and the "14n+4" rule for *nido* structures (Scheme 2).<sup>15,53</sup> Considering  $[\text{Fe}_6]^{2-}$  in a

**Scheme 2. General Formulation and Electron-Counting for Metal–Carbido Clusters of the Closo and Nido Variety Synthesized Herein and Predicted by This Work**



covalent electron-counting rationale, the carbide ( $4 e^-$ ), six iron centers ( $48 e^-$ ), 16 CO ligands ( $32 e^-$ ), and two extra electrons (dianionic,  $2 e^-$ ) afford an  $86 e^-$  cluster. This predicts a *closo*- $\text{M}_6$  structure:  $(14 \times 6) + 2 = 86 e^-$ .

Regarding  $[\text{Fe}_6]_0$ , an attempt to rationalize the same formulation of this cluster as a *closo*- $[\text{Fe}_6(\text{C})(\text{CO})_{18}]$  was unproductive: this cluster is an  $88 e^-$  formulation, while the *closo*- $[\text{Fe}_6]$  electron-counting predicts only  $86 e^-$ . An alternate explanation would be a formulation with one less CO ligand, as *closo*- $[\text{Fe}_6(\text{C})(\text{CO})_{17}]$  ( $86 e^-$ ). However, this would require the presence of a single bridging CO ligand, and no experimental or computational evidence for a truly bridging (i.e., not "semi-bridging") CO ligand was observed. Continuing with the  $[\text{Fe}_6(\text{C})(\text{CO})_{18}]$  formulation, we were enthused to find that the DFT-optimized structure for **2** was a *nido*-pentagonal bipyramid (PBP)—i.e., a PBP with one Fe missing; this cluster is, of course, also formulated as an  $88 e^-$  cluster. However, the *nido* cluster electron-counting rule for a six-metal cluster with an "open" metal site predicts  $14n + 4 = 88 e^-$ , which is in perfect agreement with both the experimental formulation and the DFT optimized structure. Indeed, the cluster electron-counting rules should provide a framework for predicting the isolability of higher nuclearity iron carbide clusters. For example, the pentanuclear PBP cluster *closo*- $[\text{Fe}_7(\text{C})(\text{CO})_{21}]$  or the related dianion *closo*- $[\text{Fe}_7(\text{C})(\text{CO})_{20}]^{2-}$  may be isolable clusters. Our continuing synthetic work in this area is testing these hypotheses, to further push the boundaries of hypervalent carbide bonding motifs.

**Relations to Nitrogenase FeMoco.** The FeMoco cofactor of nitrogenase contains a central interstitial carbon atom, and Münck and co-workers have used Mössbauer spectroscopy and DFT to better understand the effect of this species.<sup>54</sup> The

average  $\delta$  for the cofactor irons is  $0.41 \text{ mm s}^{-1}$ , which is thought to arise from a cofactor with oxidation states  $\{(\text{Mo}^{\text{IV}})(\text{Fe}^{\text{II}})_4(\text{Fe}^{\text{III}})_3\}$ . Although the isomer shift is similar to that of site 3, the coordination environment of the two clusters is significantly different; the iron centers of the nitrogenase cofactor are coordinated by sulfide ions, while those of site 3 are coordinated by carbonyls. However, these researchers calculated that the interstitial C has the effect of increasing average  $\delta$  for the irons in the FeMoco cluster by  $0.15 \pm 0.03 \text{ mm s}^{-1}$ , and this effect might be transferable to site 3. That is, the bonding interaction to the central carbide might explain, to some extent, the unusually high  $\delta$  of the site 3 irons. Münck and co-workers<sup>54</sup> also found that Fe–C interactions in FeMoco were primarily ionic in character rather than covalent. This may favor a Schrock-type Fe–C interaction, which would stabilize Fe in a higher valent state,<sup>55</sup> rather than a Fischer-type interaction, which would stabilize Fe in a lower valent state. We note, however, that the Fe–C(carbide) bond lengths found in the enzyme (all  $\sim 2.0 \text{ \AA}$ )<sup>10</sup> are approximately  $\sim 0.1 \text{ \AA}$  longer than those observed in **1**, **3**, and **4**, although the DFT-calculated Fe–C(carbide) distances in **2** ( $1.96$ – $2.02 \text{ \AA}$ ) are quite similar to that of the enzyme.

The function of the interstitial carbide in FeMoco has been the subject of great interest, but evidence supporting any proposed function is limited. Ribbe and co-workers<sup>56</sup> found that the carbide does not exchange during turnover and is not directly involved in substrate binding or turnover. Cramer and co-workers<sup>57</sup> found that the Fe–C stretching force constant associated with the FeMoco cluster was nearly 10-fold less than comparable constants in low-spin Fe clusters such as  $[\text{Fe}_4\text{C}(\text{CO})_{12}]$ , and that the nitrogenase carbide allows for structural changes upon substrate or inhibitor binding. Creutz and Peters<sup>58</sup> have suggested that the carbide controls the reactivity of the ligated iron center. They reported that the carbanion of related complexes can accommodate a significant ionic charge and thus stabilize an ionic Fe–C interaction. Theoretical calculations by Rao, Xu, and Adamo suggest that the hydrogen- and nitrogen-based substrates bind directly to the carbide, leading to a structural rearrangement.<sup>59</sup> Also, Dance has suggested that the carbide modulates the reactivity of the cluster through "coordinative allostereism".<sup>60</sup>

Our results also favor the notion that the carbide ligand is uniquely poised to control structural changes when accompanied by changes in the distribution of redox states. The concept of "deficit spending" proposed by Seefeldt, Hoffman, and Dean has been applied mainly to the P-clusters, the idea being that the P-clusters initially donate electrons (to the FeMoco and then to substrate) followed by a reduction that returns the P-clusters to their initial state.<sup>61</sup> Given our results, one could imagine the initial donation of electrons from FeMoco to substrate followed by reduction (from the P-clusters) to return the FeMoco to its initial state. This would promote a redox-dependent disproportionation of electron density in the cluster, thereby reducing the Fe's at which  $\text{N}_2$  or  $\text{H}_2$  bind while other Fe's in the FeMoco become oxidized. Through such intracuster redox disproportionations (as found in the present cluster **2**), particular iron sites in the cofactor might become unusually powerful nucleophiles/reductants, sufficiently reactive to bind  $\text{N}_2$  and reduce the triple bond in the presence of protons.

## CONCLUSION

We summarize our findings as follows:

(1) Oxidation of the known dianionic  $[\text{Fe}_6]^{2-}$  cluster with an outer-sphere reagent (ferrocene) results in the formation of the novel, neutral cluster  $[\text{Fe}_6(\mu_6\text{-C})(\text{CO})_{18}]$ , herein referred to as  $[\text{Fe}_6]^0$ .

(2) The formulation of  $[\text{Fe}_6]^0$  was supported by synthetic interconversions among dianionic and neutral hexa- and penta-iron clusters using both outer-sphere (ferrocene,  $\text{KC}_8$ ) and inner-sphere redox reagents ( $\text{FeCl}_3$ ); substantial context is provided by structural characterization of the three other iron-carbido-carbonyl clusters.

(3) Both Mössbauer spectroscopy and DFT calculations provide evidence for  $[\text{Fe}_6]^0$  as a diamagnetic cluster, in line with all other known iron-carbido-carbonyl clusters.

(4) DFT calculations and electron-counting rules support the structural assignment of  $[\text{Fe}_6]^0$  as a *nido*-pentagonal-bipyramidal cluster.

(5) The carbide is found to support an observation of unusual redox disproportionation within the cluster. While a narrow range of oxidation states is favored in the  $[\text{Fe}_6]^{2-}$  cluster ( $\text{Fe}^0$  and  $\text{Fe}^{0.5}$ ), the  $[\text{Fe}_6]^0$  cluster exhibits the quite disparate oxidation states of  $\text{Fe}^{2+}$  and  $\text{Fe}^0$ , while maintaining the core  $\mu_6\text{-C}$  motif.

(6) Overall, this suggests that while the role of the carbide in stabilizing strongly back-bonding  $\text{Fe-N}_2$  intermediates is likely critical, our results suggest that an as yet under-appreciated aspect of the carbide (as found in the nitrogenase  $\text{FeMoco}$ ) may be to facilitate the localized distribution(s) of iron oxidation states in preparation for, and during, catalysis.

## ■ ASSOCIATED CONTENT

### ● Supporting Information

The Supporting Information is available free of charge on the ACS Publications website at DOI: 10.1021/acs.inorgchem.7b00741.

Spectral figures, tables, and experimental details (PDF)

X-ray data for compound **1a** (CIF)

## ■ AUTHOR INFORMATION

### Corresponding Author

\*E-mail: [mrrose@cm.utexas.edu](mailto:mrrose@cm.utexas.edu).

### ORCID

Chris Joseph: 0000-0002-9763-5162

Michael J. Rose: 0000-0002-6960-6639

### Notes

The authors declare no competing financial interest.

## ■ ACKNOWLEDGMENTS

We gratefully acknowledge Ryan T. Pekarek (XPS) and Dr. Mrinmoy Chakrabarti (Mössbauer analysis) for assistance in obtaining and analyzing experimental data. M.J.R. acknowledges financial support from the Robert A. Welch Foundation (F-1822), Research Corporation for Scientific Advancement (Cottrell Scholar Award, RCSA 23640), the American Chemical Society (PRF 53542-DN13), and the UT Austin College of Natural Sciences. P.A.L. acknowledges funding from the National Institutes of Health (NIH GM084266). XPS data were acquired on a Kratos Ultra instrument purchased through a grant from the National Science Foundation (CHE-0618242).

## ■ REFERENCES

- Johnson, B. F. G.; Johnston, R. D.; Lewis, J. Chemistry of polynuclear compounds 14: Hexanuclear carbidocarbonylruthenium compounds. *J. Chem. Soc. A* **1968**, 2865–2868.
- Martinengo, S.; Strumolo, D.; Chini, P. Mixed-metal carbide carbonyl clusters I: Synthesis and structural characterization of di- $\mu$ -3-acetonitrile-carbido-ennea- $\mu$ -carbonyl-hexacarbonyl-polyhedro-hexarhodium,  $[\text{Cu}_2\text{Rh}_6(\text{CO})_{15}(\text{NCMe})_2] \cdot 0.5\text{MeOH}$ . *Inorg. Synth.* **1980**, *20*, 212–215.
- Hill, E. W.; Bradley, J. S. Transition-metal cluster complexes. *Inorg. Synth.* **1990**, *27*, 182–188.
- Cariati, E.; Dragonetti, C.; Lucenti, E.; Roberto, D. Tri- and Hexaruthenium carbonyl clusters. *Inorg. Synth.* **2004**, *34*, 210–214.
- Davis, J. H.; Beno, M. A.; Williams, J. M.; Zimmie, J.; Tachikawa, M.; Muettterties, E. L. Structure and chemistry of a metal cluster with a 4-coordinate carbide carbon-atom. *Proc. Natl. Acad. Sci. U. S. A.* **1981**, *78*, 668–671.
- Takemoto, S.; Matsuzaka, H. Recent advances in the chemistry of ruthenium carbido complexes. *Coord. Chem. Rev.* **2012**, *256*, 574–588.
- Muettterties, E. L.; Krause, M. J. Catalysis by molecular-metal complexes. *Angew. Chem., Int. Ed. Engl.* **1983**, *22*, 135–148.
- Ni, F.; Lee, C. C.; Hwang, C. S.; Hu, Y.; Ribbe, M. W.; Mckenna, C. E. Reduction of fluorinated cyclopropene by nitrogenase. *J. Am. Chem. Soc.* **2013**, *135*, 10346–10352.
- Rebelein, J. G.; Hu, Y.; Ribbe, M. W. Differential reduction of  $\text{CO}_2$  by molybdenum and vanadium nitrogenases. *Angew. Chem., Int. Ed.* **2014**, *53*, 11543–11546.
- Spatzal, T.; Aksoyoglu, M.; Zhang, L.; Andrade, S. L. A.; Schleicher, E.; Weber, S.; Rees, D. C.; Einsle, O. Evidence for interstitial carbon in nitrogenase FeMo cofactor. *Science* **2011**, *334*, 940.
- Lancaster, K. M.; Roemelt, M.; Ettenhuber, P.; Hu, Y.; Ribbe, M. W.; Neese, F.; Bergmann, U.; Debeer, S. X-ray emission spectroscopy evidences a central carbon in the nitrogenase iron-molybdenum cofactor. *Science* **2011**, *334*, 974–977.
- Čorić, I.; Holland, P. L. Insight into the iron–molybdenum cofactor of nitrogenase from synthetic iron complexes with sulfur, carbon, and hydride ligands. *J. Am. Chem. Soc.* **2016**, *138*, 7200–7211.
- González-Moraga, G. Main Group-Transition Metal Mixed Clusters. Carbido-Clusters. *Cluster Chemistry*; Springer-Verlag: Berlin, Heidelberg, 1993; pp 189–191.
- Moskovits, M. Organometallic Cluster Chemistry. *Metal Clusters*; John Wiley & Sons, Inc.: New York, 1986; pp 105–130.
- Mingos, D. M. P.; Wales, D. J. *Introduction to Cluster Chemistry*, 1st ed.; Prentice-Hall Inc.: Englewood Cliffs, NJ, 1990.
- Miessler, G. L.; Fischer, P. J.; Tarr, D. A. Carbon-Centered Clusters. *Inorganic Chemistry*; Pearson, 2014; pp 611–612.
- Wijeyesekera, S. D.; Hoffman, R.; Wilker, C. N. Reactivity of Transition-Metal Cluster Carbides Which Have an Exposed Carbon Atom. *Organometallics* **1984**, *3*, 962–970.
- Beno, M. A.; Williams, J. M.; Tachikawa, M.; Muettterties, E. L. Fischer–Tropsch chemistry - Structure of a seminal  $\eta$ -2-CH cluster derivative,  $\text{HFe}_4(\eta$ -2-CH)  $(\text{CO})_{12}$ . *J. Am. Chem. Soc.* **1980**, *102*, 4542–4544.
- Braye, E. H.; Dahl, L. F.; Hübel, W.; Wampler, D. L. Preparation, properties and structure of iron carbonyl carbide  $\text{Fe}_5(\text{CO})_{15}\text{C}$ . *J. Am. Chem. Soc.* **1962**, *84*, 4633–4639.
- Churchill, M. R.; Wormald, J.; Knight, J.; Mays, M. J. Synthesis and crystallographic characterization of  $[\text{Me}_4\text{N}^+]_2[\text{Fe}_6\text{CO}_{16}\text{C}^{2-}]$ , a hexanuclear carbidocarbonyl derivative of iron. *J. Am. Chem. Soc.* **1971**, *93*, 3073–3074.
- Churchill, M. R.; Wormald, J. Crystal and molecular-structure of tetramethylammonium carbide-hexadecacarbonylhexaferate(2-),  $[\text{Me}_4\text{N}][\text{Fe}_6(\text{CO})_{16}\text{C}]$ , a hexanuclear iron cluster complex with an encapsulated six-co-ordinate carbon atom. *J. Chem. Soc., Dalton Trans.* **1974**, 2410–2415.
- Tachikawa, M.; Geerts, R. L.; Muettterties, E. L. Metal carbide clusters synthesis systematics for heteronuclear species. *J. Organomet. Chem.* **1981**, *213*, 11–24.

- (23) Bradley, J. S.; Harris, S.; Newsam, J. M.; Hill, E. W.; Leta, S.; Modrick, M. A. Synthesis and molecular and electronic-structures of the  $\mu$ -4-methylidyne clusters  $[\text{Fe}_4(\text{CO})_{12}\text{C}(\text{O})\text{OCH}_3]$  – and  $[\text{Fe}_4(\text{CO})_{12}\text{C}(\text{O})\text{CH}_3]$  – An analysis of steric and bonding effects. *Organometallics* **1987**, *6*, 2060–2069.
- (24) Rossell, O.; Seco, M.; Segalés, G.; Alvarez, S.; Pellinghelli, M. A.; Tiripicchio, A.; De Montauzon, D. Iron-gold (or -mercury) carbide clusters derived from  $[\text{Fe}_6\text{C}(\text{CO})_{16}]^{2-}$ : X-ray crystal structures of  $(\text{NEt}_4)[\text{Fe}_6\text{C}\{\text{AuPPh}_3\}(\text{CO})_{16}]$  and  $[\text{Fe}_4\text{C}\{\text{AuPPh}_3\}(\text{CO})_{11}(\text{NO})]$ . *Organometallics* **1997**, *16*, 236–245.
- (25) Gourdon, A.; Jeannin, Y. Carbonayl nitrosyl clusters – Syntheses and structures of  $[\text{Fe}_5\text{C}(\text{CO})_{12}(\text{NO})]^-$ ,  $[\text{Fe}_6\text{C}(\text{CO})_{13}(\text{NO})_2]^{2-}$ , and  $[\text{Fe}_3(\text{CO})_8(\text{NO})(\text{NH})]^-$ . *Organometallics* **1986**, *5*, 2406–2410.
- (26) Bogdan, P. L.; Sabat, M.; Sunshine, S. A.; Woodcock, C.; Shriver, D. F. Anionic iron carbide carbonyl clusters with sulfurdioxide ligands. *Inorg. Chem.* **1988**, *27*, 1904–1910.
- (27) Rail, M. D.; Berben, L. A. Directing the reactivity of  $[\text{HFe}_4\text{N}(\text{CO})_{12}]^-$  toward  $\text{H}^+$  or  $\text{CO}_2$  reduction by understanding the electrocatalytic mechanism. *J. Am. Chem. Soc.* **2011**, *133*, 18577–18579.
- (28) Taheri, A.; Berben, L. A. Tailoring electrocatalysts for selective  $\text{CO}_2$  or  $\text{H}^+$  reduction: Iron carbonyl clusters as a case study. *Inorg. Chem.* **2016**, *55*, 378–385.
- (29) Devasagayaram, A.; Periasamy, M. A simple, direct synthesis of  $\text{Na}_2\text{Fe}(\text{CO})_4$ . *Transition Met. Chem.* **1991**, *16*, S03–S04.
- (30) Agilent Technologies. *CrysAlisPro Software System*; Agilent Technologies UK Ltd.: Oxford, UK, SuperNova CCD System, 2013; 1.171.37.31.
- (31) SAINT V8.27B; Bruker AXS Inc.: Madison, WI, 2012.
- (32) CrystalClear 1.40; Rigaku Americas Corp.: The Woodlands, TX, 2008.
- (33) Altomare, A.; Burla, M. C.; Camalli, M.; Casciarano, G. L.; Giacovazzo, C.; Guagliardi, A.; Moliterni, A. G. G.; Polidori, G.; Spagna, R. SIR97: A new tool for crystal structure determination and refinement. *J. Appl. Crystallogr.* **1999**, *32*, 115–119.
- (34) Sheldrick, G. M. A short history of SHELX. *Acta Crystallogr., Sect. A: Found. Crystallogr.* **2008**, *A64*, 112–122.
- (35) Spek, A. L. PLATON, A Multipurpose Crystallographic Tool; Utrecht University: The Netherlands, 1998.
- (36) Farrugia, L. J. WinGX suite for small-molecule single-crystal crystallography. *J. Appl. Crystallogr.* **1999**, *32*, 837–838.
- (37) Nguyen, A. D.; Rail, M. D.; Shanmugam, M.; Fettingner, J. C.; Berben, L. A. Electrocatalytic hydrogen evolution from water by a series of iron carbonyl clusters. *Inorg. Chem.* **2013**, *52*, 12847–12854.
- (38) Lopatin, V. E.; Varnek, V. A.; Bel'skii, V. K. Mössbauer spectroscopy study of the composition of carbido carbonyl clusters. *J. Struct. Chem.* **2002**, *43*, 608–614.
- (39) Sutton, L. E. *Table of Interatomic Distances and Configuration in Molecules and Ions, Supplement*; The Chemical Society, 1965.
- (40) Mann, J. B. *Atomic Structure Calculations II. Hartree-Fock Wave Functions and Radial Expectation Values: Hydrogen to Lawrencium*; Los Alamos Scientific Laboratory, 1968.
- (41) Lo, F. Y.-K.; Longoni, G.; Chini, P.; Lower, L. D.; Dahl, L. F. Isolation and structural characterization of the triiron undecacarbonyl dianion  $[\text{Fe}_3(\text{CO})_{11}]^{2-}$  - Stereochemical interrelationship with triiron dodecacarbonyl and triiron undecacarbonyl hydride monoanion. *J. Am. Chem. Soc.* **1980**, *102*, 7691–7701.
- (42) Cassidy, J. M.; Whitmire, K. H. Structure and Mössbauer-effect study of  $[\text{Et}_4\text{N}]_2[\text{Fe}_2(\text{CO})_8]$ . *J. Organomet. Chem.* **1992**, *427*, 355–362.
- (43) Bockman, T. M.; Cho, H. C.; Kocki, J. K. Charge-Transfer Crystals of Octacarbonyldiferrate. Solid-State Structure and Oxidation-Reduction of an Iron-Iron-Bonded Electron Donor. *Organometallics* **1995**, *14*, 5221–5231.
- (44) Florke, U. Private Communication. 2014, CCDC no. 1034565.
- (45) Gourdon, A.; Jeannin, Y. Electrochemistry and x-ray structures of the isoelectronic clusters  $[\text{Fe}_5\text{C}(\text{CO})_{15}]$ ,  $[\text{N}(\text{PPh}_3)_2][\text{Fe}_5\text{N}(\text{CO})_{14}]$  and  $[\text{NBu}_4][\text{Fe}_5\text{C}(\text{CO})_{14}]$ . *J. Organomet. Chem.* **1985**, *290*, 199–211.
- (46) Sosinsky, B. A.; Norem, N.; Shelly, J. Spectroscopic study of a series of iron carbide clusters. *Inorg. Chem.* **1982**, *21*, 348–356.
- (47) Li, F.; Basile, V. M.; Pekarek, R. T.; Rose, M. J. Steric spacing of molecular linkers on passivated Si(111) photoelectrodes. *ACS Appl. Mater. Interfaces* **2014**, *6*, 20557–20568.
- (48) Shechter, H.; Ron, M. Niedzwiedz. Mössbauer spectrometer calibration using  $^{57}\text{Fe}$  enriched metallic iron. *Nucl. Instrum. Methods* **1966**, *44*, 268–272.
- (49) Bernhardt, E.; Bley, B.; Wartchow, R.; Willner, H.; Bill, E.; Kuhn, P.; Sham, I. H. T.; Bodenbinder, M.; Bröchler, R.; Aubke, F. Hexakis(carbonyl)iron(II)undecafluorodiantimonate(V),  $[\text{Fe}(\text{CO})_6]^-[\text{Sb}_2\text{F}_{11}]_2$ , and hexafluoroantimonate(V),  $[\text{Fe}(\text{CO})_6][\text{SbF}_6]_2$ , their syntheses, and spectroscopic and structural characterization by single crystal X-ray diffraction and normal coordinate analysis. *J. Am. Chem. Soc.* **1999**, *121*, 7188–7200.
- (50) Site 4 exhibits a quadrupole doublet (the high-energy line is at 3 mm  $\text{s}^{-1}$  at 0 T in Figure 7) with parameters typical of a high-spin Fe(II) ion with predominantly O/N ligand (ref 51). The presence of this site is difficult to rationalize because the cluster is dominated by carbonyl ligands, which generally do not support such high oxidation states, and certainly not in high-spin configurations. The Fe(II) octahedral carbonyl complex  $[\text{Fe}(\text{CO})_6]^{2+}$  has been reported (ref 49), but in this case the formally Fe(II) ion is low-spin and  $\delta$  ( $-0.003$  mm  $\text{s}^{-1}$ ) is far lower than that for site 4. Another indication that site 4 was an impurity was that the high-energy line of the site 4 doublet was substantially broader than the other spectral lines associated with the cluster.
- (51) Que, L. Aspects of  $^{57}\text{Fe}$  Mössbauer spectroscopy. *Physical Methods in Bioinorganic Chemistry*; University Science Books: Sausalito, CA, 2000; pp 287–319.
- (52) Lee, Y.; Peters, J. C. Silylation of iron-bound carbon monoxide affords a terminal Fe carbyne. *J. Am. Chem. Soc.* **2011**, *133*, 4438–4446.
- (53) Wade, K. Structural significance of number of skeletal bonding electron-pairs in carboranes, higher boranes and borane anions, and various transition-metal carbonyl cluster compounds. *J. Chem. Soc. D* **1971**, 792–793.
- (54) Vrajmasu, V.; Münck, E.; Bominaar, E. L. Density functional study of the electric hyperfine interactions and the redox-structural correlations in the cofactor of nitrogenase. Analysis of general trends in Fe-57 isomer shifts. *Inorg. Chem.* **2003**, *42*, 5974–5988.
- (55) Krapp, A.; Pandey, K. K.; Frenking, G. Transition metal-carbon complexes - A theoretical study. *J. Am. Chem. Soc.* **2007**, *129*, 7596–7610.
- (56) Wiig, J. A.; Lee, C. C.; Hu, Y.; Ribbe, M. W. Tracing the interstitial carbide of the nitrogenase cofactor during substrate turnover. *J. Am. Chem. Soc.* **2013**, *135*, 4982–4983.
- (57) Scott, A. D.; Pelmenschikov, V.; Guo, Y.; Yan, L.; Wang, H.; George, S. J.; Dapper, C. H.; Newton, W. E.; Yoda, Y.; Tanaka, Y.; Cramer, S. P. Structural characterization of CO-inhibited Mo-nitrogenase by combined application of nuclear resonance vibrational spectroscopy, extended X-ray absorption fine structure, and density functional theory: New insights into the effects of CO binding and the role of the interstitial atom. *J. Am. Chem. Soc.* **2014**, *136*, 15942–15954.
- (58) Creutz, S. E.; Peters, J. C. Catalytic reduction of  $\text{N}_2$  to  $\text{NH}_3$  by an Fe- $\text{N}_2$  complex featuring a C-atom anchor. *J. Am. Chem. Soc.* **2014**, *136*, 1105–1115.
- (59) Rao, L.; Xu, X.; Adamo, C. Theoretical investigation on the role of the central carbon atom and close protein environment on the nitrogen reduction in Mo nitrogenase. *ACS Catal.* **2016**, *6*, 1567–1577.
- (60) Dance, I. Ramifications of C-centering rather than N-centering of the active site FeMo-co of the enzyme nitrogenase. *Dalt. Trans.* **2012**, *41*, 4859–4865.
- (61) Danyal, K.; Dean, D. R.; Hoffman, B. M.; Seefeldt, L. C. Electron transfer within nitrogenase: Evidence for a deficit-spending mechanism. *Biochemistry* **2011**, *50*, 9255–9263.

(62) Govindarajan, M.; Ganasan, K.; Periandy, S.; Mohan, S. DFT (LSDA, B3LYP and B3PW91) comparative vibrational spectroscopic analysis of alpha-acetonaphthone. *Spectrochim. Acta, Part A* **2010**, *76*, 12–21.